IMAU Antarctic automatic weather station data, including surface radiation balance (1995-2022)

Maurice van Tiggelen[1], Paul C.J.P. Smeets[1], Carleen H. Reijmer[1], Peter Kuipers Munneke[1], and Michiel R. van den Broeke[1]

[1]Institute for Marine and Atmospheric research Utrecht (IMAU), Utrecht University, Utrecht, The Netherlands

Correspondence: Maurice van Tiggelen (m.vantiggelen@uu.nl)

Abstract. In cooperation with multiple institutes, the Institute for Marine and Atmospheric research Utrecht (IMAU) at Utrecht University has operated automated weather stations (AWS) at 19 locations on the Antarctic ice sheet from 1995 through 2022. Besides standard meteorological measurements (pressure, temperature, humidity, wind speed & direction), these stations include measured shortwave and longwave radiation components and surface height, thereby allowing for the reliable in situ quantification of the surface energy balance (SEB) and surface mass balance (SMB) at (two-)hourly temporal resolution. This unique dataset can be used for climate model evaluation and development, for the validation of remote sensing products, for the quantification of long term climatological changes, for the interpretation of ice cores, and for process understanding in general. This paper describes the dataset and the applied measurement corrections. The total dataset contains 154 station-years of data, of which 65 % include both SEB & SMB observations, and is available at https://doi.pangaea.de/10.1594/PANGAEA.974080 (Van Tiggelen et al., 2024).

1 Introduction

The Antarctic ice sheet is the largest reservoir of freshwater, holding a global sea-level potential of 58 m (Morlighem et al., 2020), that also acts as a reliable record of the recent climate (e.g. EPICA, 2004). Due to its isolation, dry climate, and long austral winter, it also provides unique and often favourable locations for meteorological, astronomical, geophysical and upper atmosphere observations.

Reliable in situ measurements of meteorological quantities and components of the surface energy budget (SEB) are required for climate model evaluation on the Antarctic ice sheet (e.g. Van Wessem et al., 2018; Souverijns et al., 2019; Mottram et al., 2021; Kittel et al., 2021), to provide realistic atmospheric forcing for snow/firn models (e.g. Wever et al., 2022; Le Moigne et al., 2022), and to validate satellite remote sensing products (e.g. Trusel et al., 2013), but also to train or test machine learning algorithms for e.g. surface melt detection (e.g. Hu et al., 2021), to interpret ice core observations (e.g. Laepple et al., 2011), and to provide in situ estimates the sub-seasonal surface mass balance (SMB, e.g. Reijmer and van den Broeke, 2003). In addition, such in situ observations serve as a basis for process understanding, such as surface sublimation (Thiery et al., 2012; Amory, 2020), surface melt quantification (Jakobs et al., 2020), formation and burial of meltwater lakes (Buzzard et al., 2018; Dunmire et al., 2020), blue ice formation (Bintanja and Reijmer, 2001), the formation of impermeable ice slabs (Kuipers Munneke et al., 2018), and the detection of climate trends (e.g. Turner et al., 2016).

Despite the increasing need for reliable in situ measurements, automated weather station (AWS) observations are still scarce in Antarctica. The first continuous AWS observations started in 1978 (Lazzara et al., 2012) and since then, at most 146 AWS were simultaneously recording near surface meteorological variables across the continent (Wang et al., 2023). These AWS were part of one of several networks, such as the Antarctic Meteorological Research Center (AMRC) network maintained by the University of Wisonsin-Madison (Lazzara et al., 2012), the Australian Antarctic Division (AAD) network (Allison, 1998), the Italian National Program of Antarctic Research (PNRA) network (Grigioni et al., 2016), the Chinese National Antarctic Research Expedition (CHINARE) PANDA network (Ding et al., 2022), the British Antarctic Survey (BAS) network, the Japanese Antarctic Research Expedition (JARE) network (Kurita et al., 2024), the French Antarctic Program (Institut Polaire Francais-Paul Emile Victor, IPEV) network, or other similar networks maintained by different nations or organisations. These stations are shown in Figure 1 and further described in Wang et al. (2023). The number of AWS recording the near-surface radiation balance and surface height change, allowing for the estimation of the SEB and SMB, is even much more limited. Since 1995, the Institute for Marine and Atmospheric research Utrecht (IMAU), in cooperation with the Alfred Wegener Institute (AWI), the ~~British Antarctic Survey (BAS)~~BAS, the Finnish Antarctic Research Program (FINNARP), the Norwegian Polar Institute (NPI), the United States Antarctic Research Program (USARP), the Swedish Antarctic Research Program (SWEDARP), the Royal Meteorological Institute of Belgium (KMI) and the KU Leuven has been operating 19 AWS in Antarctica, of which 16 measured the radiation components allowing for a direct quantification of the entire SEB. Recently, Jakobs et al. (2020) presented a database containing SEB calculations at 8 stations from the IMAU network where surface melt occurs.

In this work we describe the dataset of measurements from all these 19 AWS that spans from 1995 through 2022. We describe the applied corrections and processing steps, ~~but we do not apply~~ and also provide a single quality flag as well as the interpolated wind speed, air temperature and specific humidity at standard heights of 10 m and 2 m above the surface using similarity theory, which allows for an easier comparison with different datasets. Although the measurements from this dataset are also partly contained in the datasets from Jakobs et al. (2020) and Wang et al. (2021), the data presented in this work have gone through an elaborate quality control and data correction strategy, which are specifically tailored for the unique combination of sensors and locations of the IMAU dataset. On the other hand, this dataset does not contain the calculation of SEB/SMB fluxes, which requires additional model calculations.

2 AWS data description

2.1 Location and installation

The location, name and period of operation of each AWS is given in Fig. 1 and Table 1. The first station (AWS10) was erected in February 1995 on Thyssen Höhe, the south dome of Berkner Island, in cooperation with the ~~Alfred Wegener Institute (AWI)~~

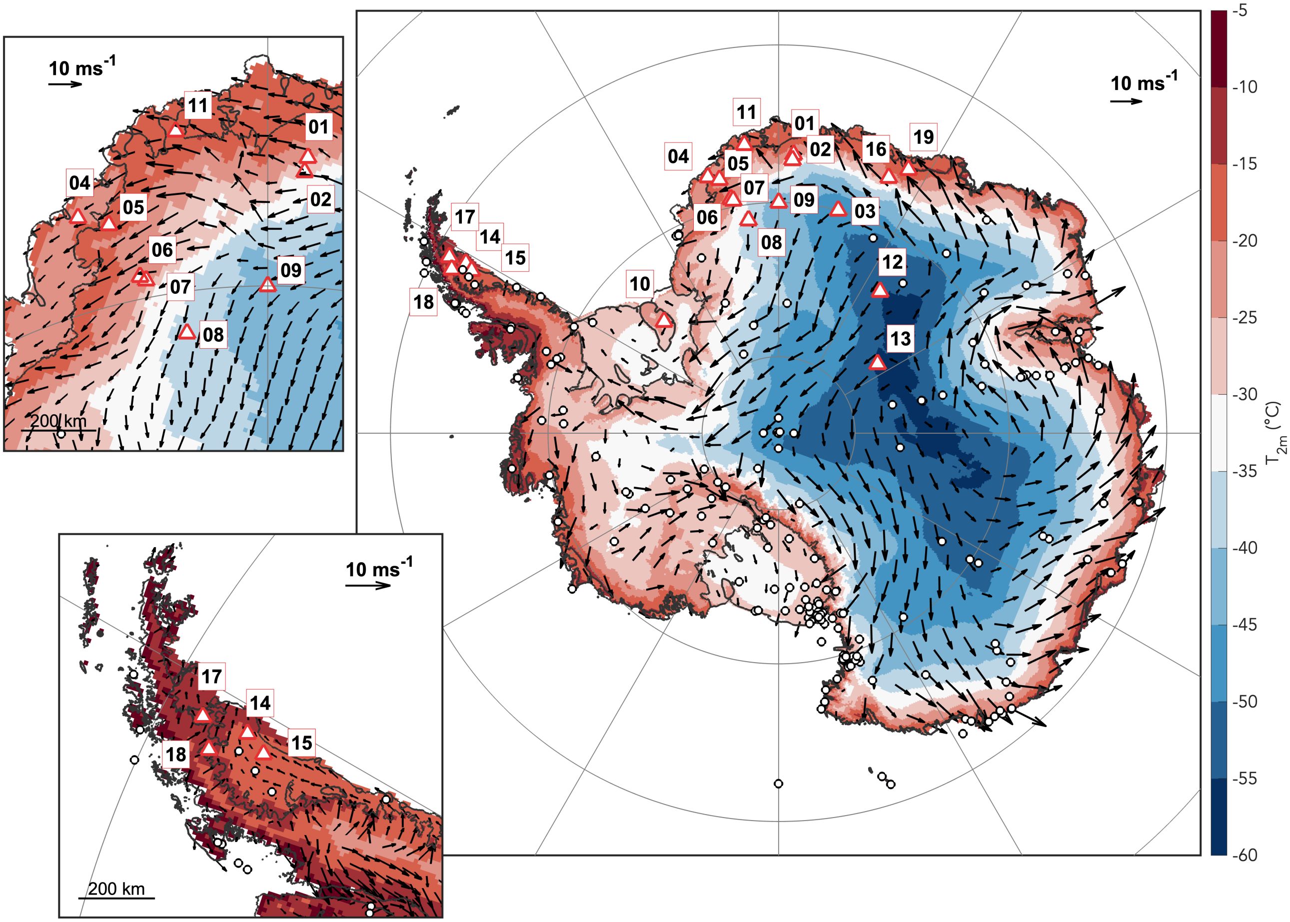

Figure 1. Location of the AWS presented in this database (red triangles). Background colour denotes the modelled annual average 2m near surface air temperature from regional climate model RACMO2.4p1 during the period 1990-2020 (van Dalum et al., 2024). Black circles denote AWS from the AntAWS database (Wang et al., 2023). Average 10m near surface wind vectors from RACMO2.4p1 are also shown. Insets are shown for Dronning Maud Land (top left) and the Antarctic Peninsula (bottom left).

~~and the British Antarctic Survey (BAS)~~ AWI and the BAS in support of paleoclimate reconstructions from deep ice coring (Reijmer et al., 1999). This AWS provided the climatological background for the medium deep ice core drilling project in 1994/95 (AWI) and the deep drilling project in 2003/05 (BAS). During the austral summer of 1996/1997, three AWS (AWS01, AWS02 AWS03) were installed in central Dronning Maud Land (DML) in collaboration with the ~~Norwegian Polar Institute (NPI)~~ NPI during the Norwegian/Swedish/Dutch NARE9697 ground traverse (Winther et al., 1997; Van den Broeke et al., 1999), as part of the European Project for Ice Coring in Antarctica (EPICA) DML pre-site survey. In the austral summer of 1997/1998, five additional AWS (AWS04-AWS08) were installed in DML in collaboration with the ~~Swedish Antarctic Research Programme (SWEDARP)~~ SWEDARP during the Swedish/Norwegian/Dutch ground traverse SWEDARP9798 (Holmlund et al., 2000), and AWS09 was installed by AWI close to the EPICA DML drilling site at AWI station Kohnen (Reijmer and van den Broeke, 2003). All these stations were part of the Netherlands contribution to EPICA (EPICA, 2006).

As part of the International Polar Year (IPY 2007-2008), AWS11 was erected in January 2007 near the top of the Halvfarryggen ice rise by AWI (Drews et al., 2013). Halvfarryggen is located about 80 km from Neumayer III station and the AWS was installed in support of a coastal deep ice core drilling project. During the austral summer of 2007/2008, one AWS was installed ~~on~~ at former Plateau Station B (AWS12) and one AWS at the pole of inaccessibility (AWS13) along the Norwegian-US scientific traverse of East Antarctica (Goldman, 2008), in collaboration with NPI and the Cooperative Institute for Research in the Environmental Sciences (CIRES). These two stations provided the climatological background in search of a favourable new deep drilling site in interior East Antarctica for drilling the oldest ice (Van Liefferinge et al., 2018). In 2009, two stations (AWS14, AWS15) were erected on the Larsen C ice shelf in collaboration with BAS, CIRES and the ~~the~~ Jet Propulsion Laboratory (Kuipers Munneke et al., 2012), followed by the installation of AWS17 in February 2011 ~~in~~ at Scar Inlet, on the remnants of the Larsen B ice shelf, and the installation of AWS18 in December 2014 in Cabinet Inlet, near the grounding line of Larsen C ice shelf (Kuipers Munneke et al., 2018).

In collaboration with the ~~Belgium Royal Meteorological Institute (KMI)~~ KMI and KU Leuven, AWS16 was installed in DML at the ~~Belgium~~ Belgian Princess Elizabeth station in February 2009 (Gorodetskaya et al., 2013), and AWS19 was installed in December 2014 near the grounding line of Roi Baudouin ice shelf, 150 km from Princess Elizabeth station (Lenaerts et al., 2017).

At present, only AWS14 ~~and~~ is still operational, and in December 2022, AWS18 ~~are still operational and~~ was reinstalled 23 km away from the grounding line due to melt pond formation complicating the yearly maintenance visits, and renamed as AWS20 which is not part of this dataset. Maintenance visits were in general performed using a standard procedure contained in a form describing a list of actions, i.e. make photographs at arrival, note anything unusual, measure yard directions and heights at arrival and departure, check datalogger data and replace the memory module. Sensors were commissioned to be replaced on a regular basis. Additional instructions and replacements were added in case of transmitted ARGOS data indicating failure of a sensor, of the datalogger, or of the power supply. AWS14 and AWS18 are part of this dataset, and were maintained by IMAU in collaboration with BAS ~~. AWS14 and AWS18 are the only type III AWS with multi-annual data on an ice shelf . These two stations~~ on the Larsen C ice shelf where they experience an average lateral displacement of 451 m year^{-1} and 193 m year^{-1} respectively due to ice flow. ~~In December 2022, AWS18 was reinstalled 23 km away from the grounding line due to melt pond formation complicating the yearly maintenance visits, and renamed to AWS20.~~ The other stations were removed, either because it was anticipated that these sites would not be visited again in the near future (AWS01-03, 06, 08, 10), or because they were funded for short project periods (AWS11, 12, 13, 14, 17). AWS04 was removed due to high accumulation rates necessitating frequent excavation, and AWS07 was removed due to frequent damage by strong winds. The continuation of AWS measurements at AWS05 was taken over by the University of Helsinki and FINNARP, and the continuation at AWS09 was taken over by AWI.

Table 1. Metadata for all the IMAU AWS in Antarctica. For stations type I & II, the locations are taken from fieldwork reports at installation date, while for stations type III the locations are from the recorded GPS position at installation date. The surface elevation is taken from the REMA DEM (Howat et al., 2022) as the average values within 500 m distance from each AWS. As of December 2022, AWS14 was still operational and AWS18 was moved 23km and renamed to AWS20. Note that AWS20 is not part of this dataset.

Station Name	Location	Latitude (°N)	Longitude (°E)	Elevation (m a.s.l)	Operation period (from – through)	AWS type	Cooperating Institute
AWS01	NARE9697 Site A	-71.900	3.083	1472	1997-01-01 – 2000-12-12	I	NPI
AWS02	NARE9697 Site C	-72.251	2.891	2419	1997-02-12 – 2000-12-13	I	NPI
AWS03	NARE9697 Site M	-75.000	15.002	3470	1997-01-28 – 2001-01-14	I	NPI
AWS04	Rampen site 1090	-72.753	-15.499	59	1997-12-19 – 2002-12-29	II	SWEDARP
AWS05	Wasa/Aboa Camp Maudheimvida	-73.105	-13.165	366	1998-02-02 – 2014-02-07	II	FINNARP/SWEDARP
AWS06	Svea Cross	-74.482	-11.517	1100	1998-01-14 – 2009-02-16	II	SWEDARP
AWS07	Scharffenbergbotnen (blue ice)	-74.578	-11.048	1175	1997-12-31 – 2003-01-06	II	SWEDARP
AWS08	Camp Victoria	-76.000	-8.0501	2398	1998-01-12 – 2003-01-07	II	SWEDARP
AWS09	Kohnen Station / EPICA DML05	-75.003	0.007	2892	1997-12-29 – 2022-11-18	II	AWI
AWS10	Thyssen Höhe, Berkner Island	-79.567	-45.782	867	1995-02-12 – 2005-07-18	I/II	AWI/BAS
AWS11	Halvfarryggen ice rise	-71.175	-6.800	700	2007-02-13 – 2019-01-31	II/III	AWI
AWS12	Plateau Station B	-78.6500	35.633	362	2007-12-15 – 2016-03-10	II	NPI/USARP
AWS13	Pole of inaccessibility	-82.117	55.033	3723	2008-01-02 – 2016-03-11	II	NPI/USARP
AWS14	Larsen C North	-67.013	-61.480	47	2009-01-21 – still running	II/III	BAS
AWS15	Larsen C South	-67.572	-62.125	49	2009-01-21 – 2014-05-06	II	BAS
AWS16	Princess Elisabeth station	-71.949	23.358	1371	2009-02-02 – 2020-07-03	II/III	KU Leuven/KMI
AWS17	Scar Inlet, Larsen B remnants	-65.933	-61.850	72	2011-02-19 – 2016-03-10	II/III	BAS
AWS18	Cabinet Inlet, Larsen C West	-66.402	-63.371	78	2014-11-25 – 2022-12-02	III	BAS
AWS19	King Baudouin ice shelf	-70.963	26.255	60	2014-12-10 – 2016-02-02	III	KU Leuven/KMI
AWS20	Cabinet Inlet, Larsen C West	-66.616	-63.229	70	2022-12-03 – still running	n.a.	BAS

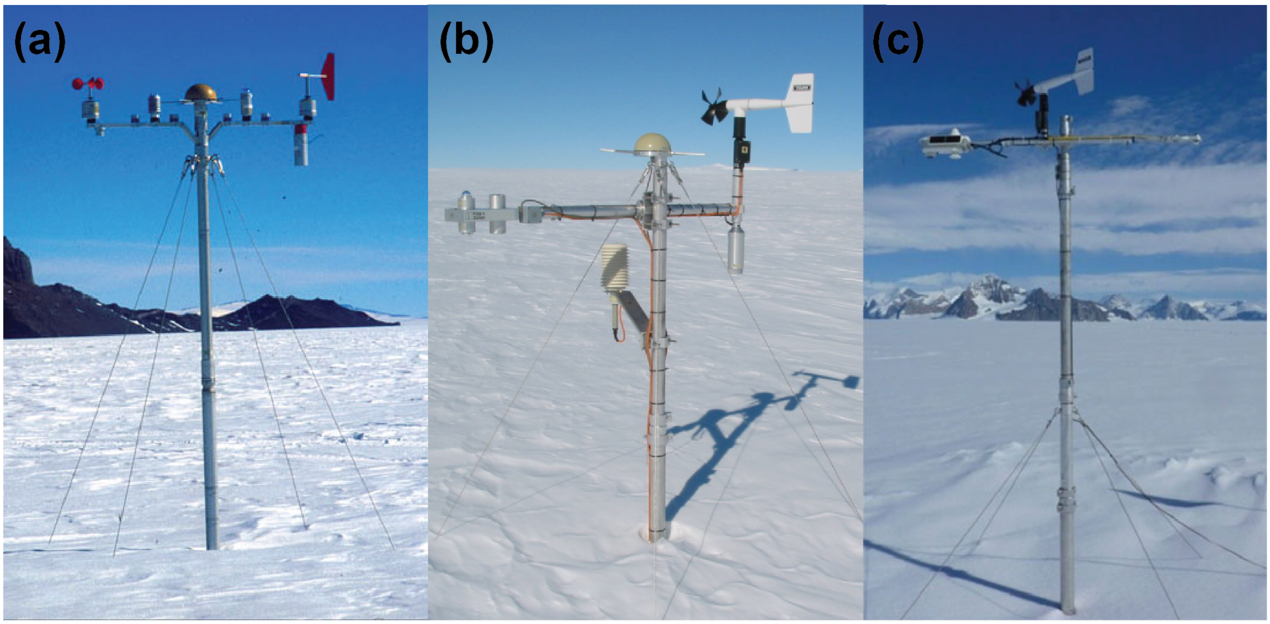

Figure 2. Photographs of the three different station types taken during maintenance visits: type I at AWS01 (a), type II at AWS06 (b) and type III at AWS18 (c).

2.2 AWS design

Since 1995, three different types of AWS designs were used. Each station consists of a four-legged frame with an extensible vertical mast consolidated by guy-wires, and a horizontal boom on which the sensors are mounted (Fig. 2). The initial installation height of the sensor boom above the surface varies across sites and between maintenance visits, and ranges between 2.6 m and 5 m. All stations measure typical meteorological parameters such as air temperature, wind speed, wind direction, downward shortwave radiation, air pressure, snow temperature and surface height, but differ in sensor specification and placement, in power supply and sampling strategy. Station types II and III were also upgraded with sensors that allow for the estimation of all the SEB components. The sensor specifications per AWS type are given in Table 2. The Type I stations (AWS01, AWS02, AWS03 and AWS10), installed during the austral summers of 1995-1996 and 1996-1997, mainly used Aanderaa sensors including a cup anemometer in combination with a wind direction vane, and did not record air humidity and only incoming shortwave radiation (Fig. 2a). The Type II station was used at most locations from austral summer 1997/98 until austral summer 2014/15 (Fig. 2b), and mainly used Vaisala sensors for air temperature, humidity and pressure, a R.M. Young wind vane for wind speed and direction, a Kipp & Zonen CNR1 radiometer for the four radiation components, and a Campbell SR50 sonic height ranger for surface height. After 2015, a more compact and ~~low-power~~ lower-power design was used at AWS11, AWS14, AWS16, AWS17, AWS18 and AWS19 (Type III, Fig. 2c), which is also referred to as intelligent weather station (iWS). These stations also ~~consist of~~ use a R.M Young wind vane and a Kipp & Zonen CNR1 or CNR4, but temperature, humidity, pressure and the surface height sensors were replaced by custom-assembled sensors in a single, compact housing. At all locations, the AWS were also fitted with thermistor strings to measure the subsurface temperatures. However, these subsurface data are not part of this quality-controlled dataset, since the exact installation depth of the subsurface sensors is not known for all maintenance visits.

The stations sample every five (Type I) or six minutes (Types II & III), after which two-hourly (Type II), one-hourly (Types I & II) or half-hourly (Type III) averages are calculated, stored locally and transmitted using Argos transmitters. The stations are powered by either lithium or alkaline batteries, in combination with a solar panel for all type III stations and for the type II station at AWS09. The sensors are neither actively ventilated nor heated to minimise power consumption and to ensure their continuous operation when left unattended for long periods of time. The measurements have never been transmitted to the Global Telecommunication System (GTS) and not been assimilated in reanalysis products.

2.3 Sensor corrections

In the following we describe the corrections applied to the dataset. Some of these are also partly described for Greenland IMAU AWS data by Smeets et al. (2018) , but have been adapted for the specific sensors and design used in this dataset. The corrections are applied separately for each station and each period of data available in between maintenance visits to accommodate the replacement or repair of sensors, and changes in sensor orientation and heights. All unheated meteorological instruments operating in polar conditions may suffer from riming or hoar frost deposition, which we assume to occur when the relative humidity exceeds 90 %, the air temperature is lower than 0°C and the absolute value of the net longwave radiation is smaller than 2 Wm^{-2} for at least 24 consecutive hours. These observations are flagged but are not removed from the dataset.

Table 2. Instruments used for the different types of IMAU AWS stations. The years denote the approximate period of operation per AWS type.

AWS	Variable	Instrument or sensor	Range	Accuracy*
	Air temperature	Aanderaa 2775C	-90 to +30 °C	0.1 °C at -20°C
	Air pressure	Aanderaa 2775C	600 to 1024 hPa	0.5 hPa
Type I	Wind speed	Aanderaa 2740	0.5 to 76 ms^{-1}	0.5 ms^{-1}
	Wind direction	Aanderaa 2750	0 to 360 °	5 °
1995-1997	Shortwave radiation	Aanderaa 2770	300-2500 nm, 0 to 2000 Wm^{-2}	< 20 Wm^{-2}
	Snow temperature	Aanderaa	-70 to +30 °C	0.1 °C
	Surface height	Aanderaa	1 to 4 m	0.01m
	Datalogger	Campbell CR10	-	-
	Air temperature	Vaisala HMP35AC	-80 to +56 °C	0.3 °C
	Relative humidity	Vaisala HMP35AC	0 to 100 %	2 % (RH <90 %)
	Air pressure	Vaisala PTB101B	600 to 1060 hPa	0.5 hPa
	Wind speed	R.M. Young 05103	0 to 60 ms^{-1}	0.3 ms^{-1}
Type II	Wind direction	R.M. Young 05103	0 to 360 °	3 °
	Shortwave radiation	Kipp & Zonen CNR1	305-2800 nm	10 % daily totals
1998-2014	Longwave radiation	Kipp & Zonen CNR1	5-50 μm	10 % daily totals
	Snow temperature	Vaisala HMP35AC	-80 to +56 °C	0.3 °C
	Surface height	Campbell SR50	0.5 to 10 m	0.01m or 0.4 %
	Air temperature 2**	Campbell PT100	0.5 to 10 m	0.1 °C
	Datalogger	Campbell CR10	-	-
	Air temperature	NTC thermistor	-60 to 40 °C	0.1 °C
	Relative humidity	Sensirion SHT25	0 to 100 %	1.8 %
	Air pressure	Freescale Xtrinsic MPL 3115A2	200 to 1100 hPa	4 hPa
	Wind speed	R.M. Young 05103	0 to 60 ms^{-1}	0.3 ms^{-1}
Type III	Wind direction	R.M. Young 05103	0 to 360 °	3 °
	Shortwave radiation	Kipp & Zonen CNR4	300-2800 nm	< 5 % daily totals
2015-2023	Longwave radiation	Kipp & Zonen CNR4	4.2-42 μm	10 % daily totals
	Snow temperature	PS222J2	-80 to +56 °C	0.1 °C
	Surface height	MaxBotix HRXL-MaxSonar-WRS	0.5 to 5 m	0.01m or 0.4%
	Tilt	HMC6343	-179.9 to 179.9 °	0.1 °
	Datalogger	Custom-made at IMAU	-	-

* Reported accuracy by the manufacturer

** The PT100 air temperature sensor is only installed on AWS09 after Jan 2008 and at AWS12 and AWS13

Temperature correction

The heating of the temperature sensor in the passively ventilated radiation screens causes an excess temperature, which peaks during conditions with high insolation and low wind speeds. The correction is empirically determined per station type by comparing with measurements from a separate thin wire thermocouple corrected for radiation errors, following Jacobs and McNaughton (1994) and Smeets et al. (2018). For stations type I & II, we use simultaneous measurements of a 0.003 inch fine-wire thermocouple (Campbell FW3 Type E) and HMP35 probe (Vaisala) inside a Young multi-plate radiation shield during August 2003 to August 2004 at location S6 on the Greenland ice sheet (Smeets et al., 2018) to fit the excess temperature to the following empirical relation:

$$\Delta T = \frac{SW_{tot}}{A(12U)^{1.3}}, \tag{1}$$

with ΔT the excess temperature correction that is subtracted from the raw measurements, $SW_{tot} = SW_d + SW_u$ the total measured shortwave radiation, SW_d/SW_u the downward/upward shortwave radiation, A a geometry factor that depends on the sensor and radiation shield, and U the horizontal wind speed at sensor height. For AWS Type II, $A = (9.59\ 10^{-3} SW_{net} + 6.32)/17$, which is determined empirically based on data from S6. We also use this relation for stations type I since no information on radiation shield characteristics is available. At very low wind speeds (U < 2 m s^{-1}), we estimate ΔT from interpolating between points $\Delta T(U = 0)$ and $\Delta T(U = 2)$, with $\Delta T(U = 0) = k \times 4.14 \times 10^{-3} - 0.15$. An example of the temperature excess is shown in Fig. 3a, in which the uncorrected ~~hut temperature~~ temperature measured in the radiation shield is compared to uncorrected thermocouple measurements for various wind speeds and values of total shortwave radiation. The accuracy of the temperature excess correction is deemed better than 1 $°C$ for wind speeds exceeding 1 m s^{-1}.

Type III stations have different radiation shields than previous types, and have sufficient reference thermocouple measurements available that allow for a different, more automated correction procedure. The procedure is based on Nakamura and Mahrt (2005) and Huwald et al. (2009). The temperature excess is fitted to the following non-dimensional quantity:

$$C = 1000 \frac{SW_{tot}}{\rho_a C_p U T}, \tag{2}$$

where ρ_a is the air density and C_p the air specific heat capacity at constant pressure. The temperature excess is fitted to the non-dimensional quantity C with a first order and a third order polynomial using measurements from an additional thermocouple corrected for heating, if available, or using the results from multiple other stations equipped with thermocouples and the same radiation shield. The first-order polynomial is used for large ΔT values, in order to prevent an unrealistic correction for very low winds speeds and high insolation (i.e. C < 8).

On average, this correction reduces the measured air temperature between 0 to 1 K at all AWS, but may reach up to 6 K during brief periods with both high insolation, low wind speeds and less effective radiation shields (Fig. 3b).

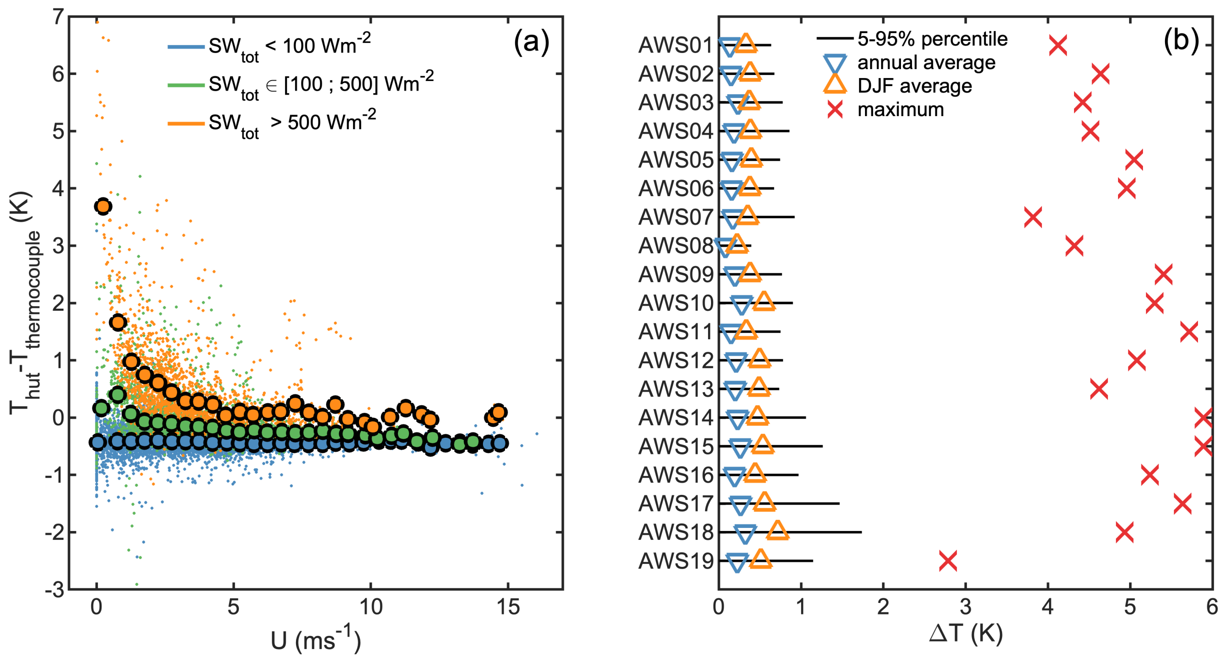

Figure 3. (a) Example of temperature excess versus horizontal wind speed for three different classes of total shortwave radiation ($SW_{tot} = SW_d + SW_u$) at AWS14 in the period December 2019 - October 2020 when an additional thermocouple measurement was available. Note that a bias of about -0.4 °C is still present in the thermocouple readings. (b) Annual average (blue triangles), DJF average (orange triangles), annual maximum (red crosses) and 5-95% percentile range (black lines) of the correction for solar heating of the temperature ~~hut~~ in the radiation shield during the entire measurement period per station.

Relative humidity

The hygrometers measure relative humidity with respect to liquid water, hence their output needs to be rescaled to relative humidity with respect to ice. Furthermore, we rescale the humidity values for temperatures below 0°C such that the highest RH values, deemed close to saturation, are also close to 100 % measured relative humidity. We employ a similar method as described by Anderson (1994). At the end of the correction procedure, we also correct for the fact that the relative humidity was measured inside an excess heated radiation shield instead of the ambient air.

The procedure we employ is as follows. First, we bin the raw, uncorrected RH values in 1 $°C$ windows using the raw, uncorrected air temperature, and we keep the 95th highest percentile values per bin if at least 20 values are present. Then, we first try a second order fit for all data up to -4$°C$, and if the curvature of the fit is positive, i.e. when the upper bound of RH values increases for very low temperatures, we use a linear fit instead. Additionally, for stations where the minimum air temperature bin lies below -60 $°C$, we determine a second linear fit for all air temperature values up to -55 $°C$. The latter allows for some overlap between the two fits around -60 $°C$. The reason for the different fits are the varying sensor characteristics over the vast temperature range encountered within the dataset, ranging from the coastal stations up to the Antarctic plateau. The polynomials are then rescaled using the RH offset at 0 $°C$ compared to 100 %. The resulting functions determine the upper bound of the raw RH measurements versus air temperature, which are used to select data found within $\pm$ 1 % of these curves. We recalculate the raw RH values into their values over ice, and then fit a fourth order polynomial that is used to re-scale the RH value to 100 % over the entire temperature range, the same as is done in Anderson (1994).

The final step is the correction due to different saturated water vapour pressures in the ~~hut~~ radiation shield and in the ambient air (e.g. Makkonen and Laakso, 2005) which is only applied to RH values lower than 98 % in order to prevent the correction to result in RH values far above 100 %.

Pyrgeometer (longwave radiation)

~~Readings~~ If not affected by rime of frost, readings from an unventilated pyrgeometer are affected by (1) window heating due to absorption of solar radiation, (2) instrumental biases, and (3) the emission of longwave radiation in the air column between the surface and the sensor under conditions of strong vertical temperature gradients .

First, we correct for window heating in the following empirical way, based on measurements taken during an intercomparison experiment at the Baseline Surface Radiation Network (BSRN) site of the Royal Netherlands Meteorological Institute (KNMI) located at Cabauw, in the Netherlands (Knap, 2022). The results illustrated a dependence of window heating on sensor type (CNR1 or CNR4), shortwave radiation heating the window, and wind speed cooling the window, which is also confirmed by stations presented in this dataset (Fig. 4a). The window heating effect can be described as a ratio between incoming shortwave radiation and wind speed:

$$\Delta LW_{u,d} = a\frac{SW_{u,d}}{U^b}, \quad (3)$$

with a a sensitivity coefficient for window heating that depends on the sensor type (0.025 for model CNR1 and 0.0125 for model CNR4), $b = 0.35$ a sensitivity coefficient to wind speed cooling, and $\Delta LW_{u,d}$ the window heating correction that is computed for both longwave components separately and subtracted from the raw measurements.

Then, we correct for instrumental biases using the following procedure. ~~Per~~ For each station we select measurements with SW_d lower than 50 $\mathrm{Wm^{-2}}$ to rule out any influence from window heating. We use a twofold method depending on data availability within the temperature range. The correction is illustrated in Fig. 4b.

For stations where there are no remaining data with T > 0 °C, we further only select the data during near-neutral conditions to minimise the influence of temperature effects. ~~These are wind speeds~~ Near-neutral conditions are defined as when wind speeds are higher than 6 $\mathrm{ms^{-1}}$, relative humidity above 80 %, temperatures below -10 °C and a temperature difference between the ambient air and the radiometer body smaller than 0.5 °C. We define the bias as the median of the remaining LW_u - σT^4 data, with T the air temperature and $\sigma = 5.67 \times 10^{-8}$ $\mathrm{Wm^{-2}K^{-4}}$ the Stefan-Boltzmann constant. We assume that LW_d has the same offset, so the bias is then subtracted from the entire dataset for both longwave components.

For stations with remaining data with T > 0 °C, we bin all the LW_u data for $SW_d < 50$ $\mathrm{Wm^{-2}}$ as function of air temperature in windows of 0.2 °C, and compute the median of the 5 largest values within each bin. We then compute the linear regression of these maxima versus air temperature, and define the bias as the intercept of the linear fit for T = 0 °C. We interpret this bias as instrumental error, hence we subtract it from the entire dataset for both longwave components. In addition, we interpret the remaining linear offset for T > 0 °C as longwave radiation divergence, hence we also remove/add this linear dependency from the measured LW_u/LW_d, respectively, in order to obtain measured longwave radiation components at the surface.

When averaged over the entire time series per station, and including both the correction for window heating, instrumental bias and longwave radiation divergence, the downward longwave radiation component is reduced by between 0 and 10 $\mathrm{Wm^{-2}}$ (Fig. 4c). The largest correction of 40 $\mathrm{Wm^{-2}}$ is found at AWS17 during a co-occuring period with both high air temperature and large insolation. Type III stations have the largest correction, partly due to their geographical location on ice shelves, but also due to a different instrumental offset compared to type II.

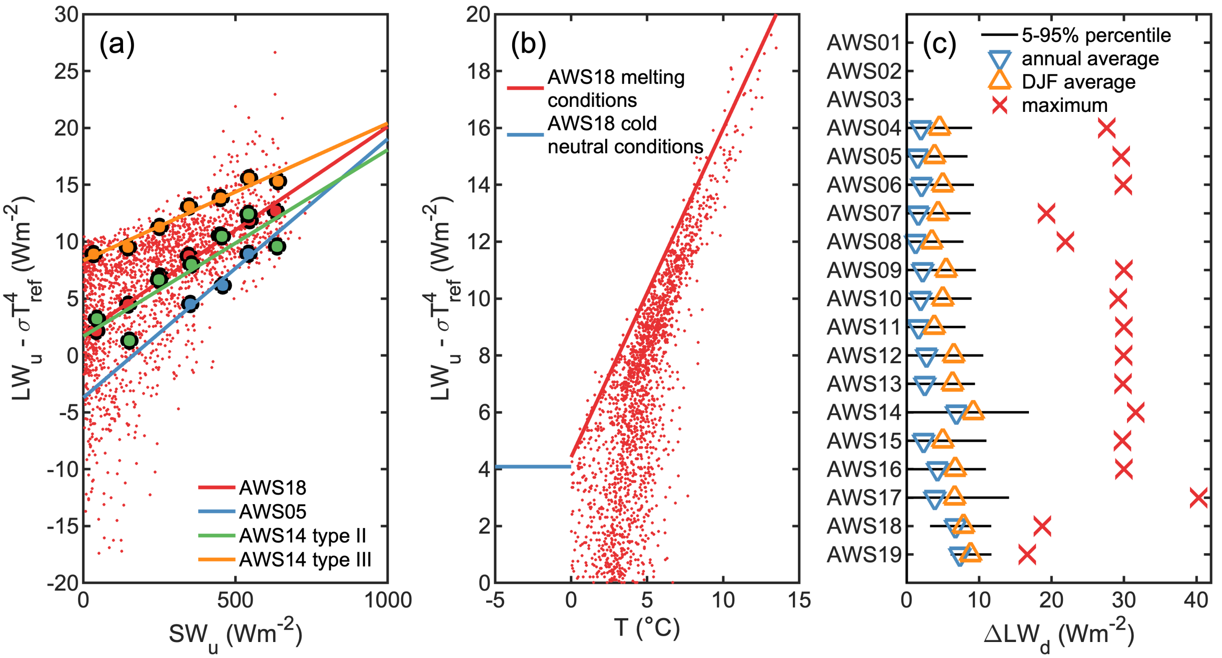

Figure 4. (a) Pyrgeometer window heating: excess upward longwave radiation versus upward shortwave radiation, and corresponding bin averages and linear regressions for daytime data when solar zenith angles are below 90 degrees and when air temperatures are in the range $[2-5]^{\circ}C$. (b) Sensor bias and emitted longwave radiation by the air: excess upward longwave radiation versus air temperature for nighttime melting conditions data (red) and nightime cold neutral conditions (blue) at AWS18, and corresponding linear regressions. (c) Annual average (blue triangles), DJF average (orange triangles), annual maximum (red crosses) and 5-95 % percentile range (black lines) of the correction for downward longwave radiation during the entire measurement period per station.

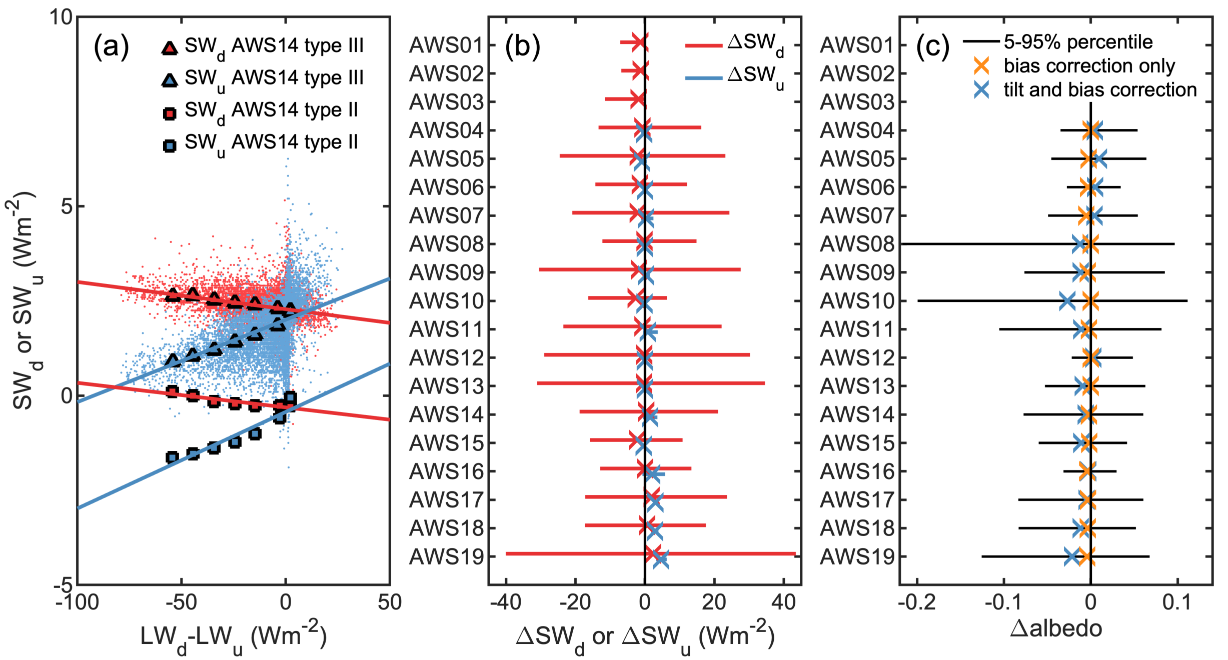

Figure 5. (a) Pyranometer zero-offset: measured shortwave radiation components versus measured net longwave radiation, and corresponding bin-averages and linear regression. Only nighttime data for solar zenith angles above 110 degrees are shown. (b) Average (crosses) and 5-95th percentile range (lines) of the correction for both components of shortwave radiation during the entire measurement period per station. (c) Average (crosses) and 5-95th percentile range (lines) of the impact of the pyranometer bias and tilt correction on the hourly measured broadband shortwave albedo, only computed for data when the solar zenith angle is lower than 70 degrees.

Pyranometer (shortwave radiation)

~~The~~ If not affected by rime of frost, the pyranometers used to measure shortwave radiation suffer from a zero-offset due to net infrared cooling of the sensor, and from tilt due to the imperfect levelling of the sensor boom. We correct for the zero-offset using the following procedure. Per sensor we select nighttime periods with solar zenith angles larger than 110 degrees, and bin the recorded shortwave components as function of net longwave radiation in windows of 5 $\mathrm{Wm^{-2}}$. We then fit an empirical linear regression to the averages in each bin, as described in Behrens (2021). An example of this procedure is shown in Fig. 5a. The correction is written as:

$$\Delta SW_{u,d} = a_{u,d} LW_{net} + b_{u,d} \tag{4}$$

with $\Delta SW_{u,d}$ the correction for either downward or upward shortwave radiation that is subtracted from the raw measurements, $LW_{net} = LW_d - LW_u$ the net recorded longwave radiation and $a_{u,d}$ and $b_{u,d}$ empirically derived parameters of the linear regression that depend on the location and AWS type. This correction is then assumed to be valid continuously and is therefore applied to the entire dataset. On average, this correction does not exceed 5 $\mathrm{Wm^{-2}}$ (Fig. 5b).

To correct for the imperfect levelling of the AWS, we use the same empirical correction procedure for all stations, which is described by Van den Broeke et al. (2004). The method assumes that the measured daily totals in upward shortwave radiation are not affected by sensor inclination. An hourly "accumulated" albedo is then computed using the 24-hour moving total SW_u and SW_d centred around the time of observation, which is then used to correct the hourly SW_d from the hourly measured SW_u. This method was chosen for consistency and deemed most adequate given the lack of regular direct tilt measurements during AWS maintenance and varying tilt angles over time. However this method effectively removes the daily-cycle in albedo. An alternative method is proposed by Wang et al. (2016) but was not applied to this dataset since this method requires knowledge of clear-sky days and a modelled surface radiation on these clear days.

The correction for both shortwave components ranges between -5 and 5 Wm^{-2} on average, but varies between -40 and 40 Wm^{-2} for the downward component due to tilt (Fig. 5b). This correction also affects the estimated broadband shortwave albedo between -0.02 and 0.01 on average depending on the station (Fig. 5c), but may reach between -0.2 to 0.1 at e.g. AWS08 and AWS10. Only a marginal fraction of the albedo correction is due to the zero-offset.

Sonic height ranger

The readings from the sonic height ranger are corrected for the temperature dependence of the speed of sound according to:

$$H_{corr} = H_{raw}\sqrt{\frac{T}{273.15}}, \tag{5}$$

with H_{corr} and H_{raw} the corrected and raw signals, and T the air temperature in K. The influence of humidity on the speed of sound is neglected due to the low humidity values and slower variation in air specific humidity.

2.4 Data processing/quality control

Filtering

Each measured variable is filtered using a threshold filter with bounds manually fixed to remove unrealistic values (Table A1). In addition, the measurements from the sonic height ranger are filtered with manually set thresholds that vary in time, after which the remaining individual spikes in the data are automatically removed using a moving median absolute difference filter. When no measurements are available from the data logger, either due to logger failure, corrupted or missing data, or lack of maintenance visits, the data transmitted using Argos satellite communication are used instead, which are filtered for corrupted data generated by the satellite transmission . The data during periods with known logger/power supply issues, or when the AWS structure was damaged by wind or buried by accumulation are also manually removed from the dataset. The dataset also contains a time series of filtered surface height after applying a daily moving average filter, which is used to estimate cumulative height change. The height of the sensor boom is manually reset during each maintenance visit, and then estimated using the daily-averaged filtered measurements from the sonic height ranger.

Derived variables

The list of variables contained in the dataset is given in Table 3. The specific humidity is computed as:

$$q_v = \frac{RH}{100} q_s \tag{6}$$

with RH the corrected measured relative humidity in percentage, and q_s the equilibrium or saturated specific humidity, computed as:

$$q_s = (R_d/R_v)\frac{e_s}{(p+e_s(R_d/R_v-1))}, \tag{7}$$

with $R_v = 461.5 Jkg^{-1}K^{-1}$, $R_d = 287.05 Jkg^{-1}K^{-1}$ the gas constants for water vapor and dry air, respectively, p the air pressure and e_s the equilibrium water vapour pressure. The Magnus formula over ice is chosen for e_s, as given by WMO (2023) :

$$e_s = 6.112 \exp\left[\frac{22.46T}{272.62+T}\right], \tag{8}$$

with T the air temperature in degrees centigrade, which is valid down to -65 °C. This relationship is also used in this dataset for temperatures below this range, but should be used with caution.

Correction to standard heights

The air temperature, specific humidity and wind speed, corrected to standard heights above the surface, are also given in order to allow for an easy comparison between stations and with atmospheric models. Assuming validity of Monin-Obukhov similarity theory, the quantities at standard heights are written:

$$u_{10m} = \frac{u_*}{\kappa}\left[\ln\left(\frac{10}{z_{0m}}\right) - \Psi_M\left(\frac{10}{L}\right) + \Psi_M\left(\frac{z_{0m}}{L}\right)\right], \tag{9}$$

$$T_{2m} = T_s + \frac{\theta_*}{\kappa}\left[\ln\left(\frac{2}{z_{0T}}\right) - \Psi_H\left(\frac{2}{L}\right) + \Psi_H\left(\frac{z_{0T}}{L}\right)\right] - \frac{2g}{C_p}, \tag{10}$$

$$q_{2m} = q_s + \frac{q_*}{\kappa}\left[\ln\left(\frac{2}{z_{0q}}\right) - \Psi_Q\left(\frac{2}{L}\right) + \Psi_Q\left(\frac{z_{0q}}{L}\right)\right], \tag{11}$$

where z_{0m} is the roughness length for momentum that is taken as a constant value of 10^{-4} m, and z_{0T}/z_{0q} are the scalar roughness lengths, which are parameterized after Andreas (1986). T_s is the recorded surface temperature, and q_s is the saturation specific humidity for $T = T_s$. $\kappa = 0.4$ is the Von Kármán constant and $g = 9.81$ ms^{-2} the gravitational acceleration. The Obukhov length L, as well as the fluxes $u_* = \sqrt{-\overline{u'w'}}$, $T_* = -\overline{w'T'}/u_*$, and $q_* = -\overline{w'q'}/u_*$ are computed using the bulk flux method implemented in the surface energy balance model described in Van Tiggelen et al. (2023), using the variable height of the sensors. The relations from Holtslag and De Bruin (1988) for the integrated stability functions Ψ_M,Ψ_H and Ψ_Q are used. The quantities at standard heights are only available when measurements of both the surface height and all four components of net radiation are not flagged.

Table 3. Descriptions of variables in the dataset

Variable label	Unit or format	Description
time	yyyy-MM-dd HH:mm:ss	UTC time at the end of the measurement interval
t	$^{\circ}C$	air temperature at boom height
t2m	$^{\circ}C$	air temperature corrected at 2m height using similarity theory
q	g kg^{-1}	specific humidity at boom height
q2m	g kg^{-1}	specific humidity corrected at 2m height using similarity theory
rh	$\%$	relative humidity at boom height
rh2m	$\%$	relative humidity corrected at 2m height using similarity theory
wspd	ms^{-1}	horizontal wind speed at boom height
wspd10m	ms^{-1}	horizontal wind speed corrected at 10m height using similarity theory
wspdmax	ms^{-1}	maximum wind speed at boom height
wdir	$^{\circ}$	Wind from direction, positive clockwise with respect to true North
p	hPa	Air pressure
SWd	Wm^{-2}	downwards shortwave radiation
SWu	Wm^{-2}	upwards shortwave radiation
LWd	Wm^{-2}	downwards longwave radiation
LWu	Wm^{-2}	upwards longwave radiation
z_surf	m	Unfiltered sonic height ranger measurement
z_surf_filtered	m	Filtered sonic height ranger measurement
cum_surface_height_zboom	m	Cumulative change in surface height since start from sonic height ranger on boom
LAT	decimal degrees	Latitude
LON	decimal degrees	Longitude
alb	-	Broadband shortwave albedo for solar zenith angles lower than 70 degrees
Ts_obs	$^{\circ}C$	Observed surface temperature assuming an emissivity of 1
errorflag	rabcdefhgi	quality flag, see Sect. 2.4 and Table 4. 1000000000 for non-suspicious data

Flagging

A binary quality flag is generated for each sample that aims to incorporate all the possible combinations of suspicious or missing data for each measured variable and possible riming or hoar frost deposition, hereafter denoted 'riming', in one parameter (10 combinations). The flag is formatted as a combination of 10 consecutive 1 or 0's in order "rabcdefghi", where a numerical value of 1 denotes a suspicious or missing sample for a specific variable, and a numerical value of 0 denotes a seemingly, properly functioning sensor. An exception is for the first value ("r") that can have a value of 1 (no suspected riming) or 2 (suspected riming or cannot be excluded), in order to prevent an errorflag value with 10 consecutive 0's. The second to last binary flags are in respective order related to the following measurements: a) the surface height, b) air pressure, c) specific humidity, d) air temperature, e) outgoing longwave radiation, f) incoming longwave radiation, g) outgoing shortwave radiation, h) incoming shortwave radiation and i) wind speed. The specific conditions for which each flag is raised per variable are given in Table 4. In summary, valid samples when all the sensors seem to function properly at the same time have a value of 1000000000. The resulting quality parameter allows for straightforward data selection or interpolation routines, which was not done in this dataset.

3 Data availability and range

The period covered by the dataset is shown in Fig. 6, and the number of valid, non-flagged samples per variable and per station is given in Table B1. In total, 56157 days ($\approx$ 154 years) of data are available from 1995 through 2022, out of which 36418 days ($\approx$ 100 station-years, or 65 %) of data with both meteorological observations, sonic height ranger measurements and all four components of net surface radiation (Fig. 6). AWS09 has the longest time series (24.9 years), while AWS05 contains the longest continuous time series of full AWS & SEB data (11.6 years). At AWS09, the outgoing longwave radiation is missing between 2009 and 2016 due to a malfunctioning logger, while from 2017 onwards, the relative humidity is missing due to a malfunctioning sensor. This means that not more than one year of interpolated temperature data is available at AWS09 after 2009, since all variables need to be un-flagged to reliably interpolate quantities using Eqs. 9-11. At the plateau sites AWS12 and AWS13, no pressure data is available due to a malfunctioning datalogger, and no wind speed and wind direction data is available after 70 days of operation at AWS13 due to a malfunctioning sensor. Yet, despite the very cold and dry climate, most other variables including surface height are available for the entire period at AWS12 and AWS13. The Type III AWS have the highest success rate (95 %). Data gaps longer than several days often affect all the variables, either due to a malfunctioning logger or power supply (e.g. AWS14 during 2017), or due to the AWS being buried by snow (AWS11 in 2012). Long periods of longwave radiation measurements are flagged at the plateau stations AWS09, AWS12 and AWS13 during winter, since the radiometers function well below their operation temperature range, but are not removed from the dataset.

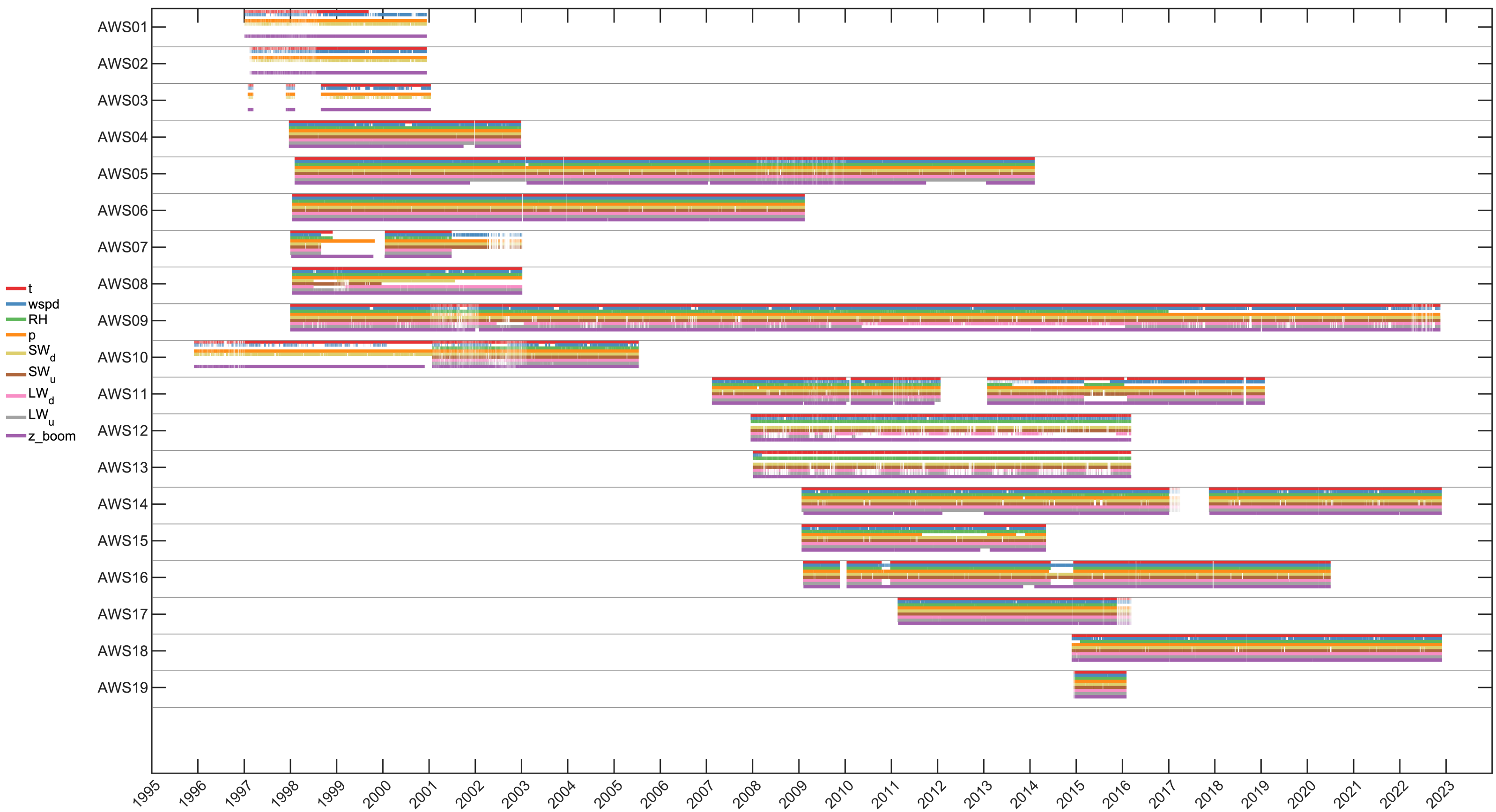

Figure 6. Availability of non-flagged hourly data per station. Each colour denotes a different variable. The number of non-flagged data per station and in total is also given. The number of non-flagged samples per variable and per station is given in Table B1.

Table 4. Procedure for making the single quality parameter "errorflag" for flagging suspicious or missing data. TOA = Top of Atmosphere.

parameter in "errorflag" (rabcdefghi)	description or flagged suspicious sample	condition when flag raised
r = 2	riming suspected or cannot be excluded, or sensors are (close to) being burried	$\lvert LW_{net} \rvert$ < 2 Wm^{-2} and RH > 90 % and $T < 0°C$ for at least 24 consecutive hours, or any of these parameters are missing, or z_surf < 0.2 m
a = 1	z_surf	z_surf missing or outside the manually fixed interval
b = 1	p	p missing
c = 1	q	RH missing, or RH > 110 %
d = 1	t	t missing
e = 1	LWu	LWu missing, or LWu > 320 Wm^{-2}, or $T < -60°C$
f = 1	LWd	LWd missing, or LWu > 320 Wm^{-2}, or $T < -60°C$
g = 1	SWu	SWu missing, or daily total SWd exceeds TOA radiation, or daily total SWu is equal to zero when daily maximum TOA exceeds 10 Wm^{-2}
h = 1	SWd	SWd missing, or daily total SWd exceeds TOA radiation, or daily total SWd is equal to zero when daily maximum TOA exceeds 10 Wm^{-2}
i = 1	wspd	wspd missing, or wspd < 0.1 ms^{-1} for at least 6 consecutive hours

The ~~time-averaged~~ time-averages of all measurements of incoming radiation, air temperature, wind speed and surface height change are plotted as a function of station elevation in Fig. 7, and the averages of all variables per station and per season are given in Table C1. On average, annual downward longwave radiation decreases with elevation from 230 Wm^{-2} at the ice shelf locations, to 100 Wm^{-2} at the plateau stations. The decrease in incoming longwave radiation is compensated by a similar increase in incoming shortwave radiation from about 130 Wm^{-2} near sea-level up to 200 Wm^{-2} on the Antarctic plateau. The range of yearly averaged air temperature contained in this dataset is [-55;-15] °C. The lowest daily average temperature at sensor height of -82.9 °C was recorded at AWS13 (Pole of inaccessibility) on 11 August 2010, and the highest daily averaged air temperature at sensor height of 10.2 °C recorded at AWS18 (Cabinet Inlet, Larsen C ice shelf) on 26 May 2016. Above melting temperatures occurs at 10 out of 19 stations, either on ice shelves (AWS04,14,15,17,18,19) or close to ice shelves (AWS05) , but also rarely at higher elevations on the grounded ice sheet (AWS06,07,16). The annual averaged wind speed at sensor height ranges between 3 and 8 ms^{-1}, with maximum daily averages ranging from 11.4 ms^{-1} at AWS12 (Plateau ~~sration~~ station B) up to 32.3 ms^{-1} at AWS05 (Wasa/Aboa Camp Maudheimvida). The surface height change ranges between 92 mm per year of ice ablation at Scharffenbergbotnenthe blue ice location AWS07, up to 2242 mm of snow accumulation per year at the Halvfarryggen ice rise location AWS11.

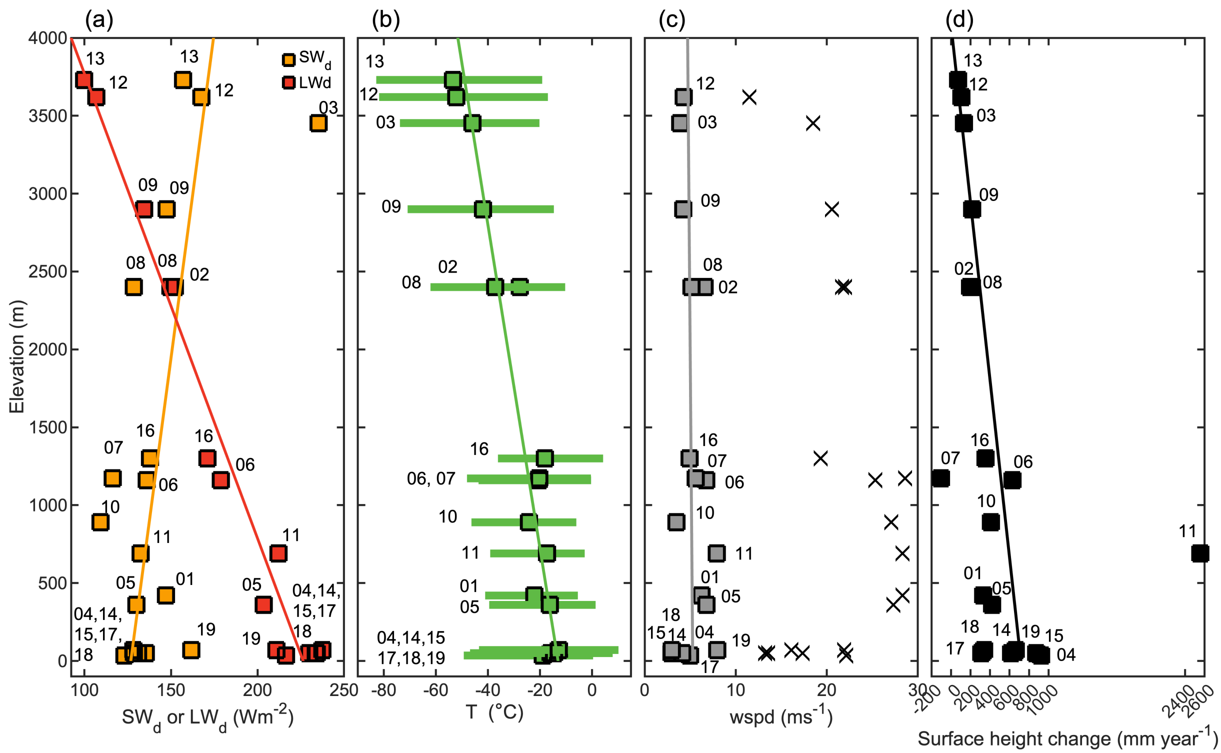

Figure 7. (a) averaged downwards shortwave radiation (yellow), downward longwave radiation (red), (b) average (squares) and minimum-maximum (lines) daily air temperature (c) average (squares) and daily maximum (crosses) wind speed, (d) average increase in surface height for all the stations during the entire measurement period. Data are only shown when at least 50 % of data are available in the entire measurement period. Solid lines denote the linear regression versus elevation. The number of each AWS is also shown.

4 Example application: inter-station correlation

An example application of this dataset is presented that takes advantage of the correlation of the measured variables between nearby stations, in order to spatially interpolate point measurements or design the optimal AWS network. The daily averaged measurements of temperature, wind speed, and both downward radiation components for January are selected. The correlation of each of these four variables is then computed for all station pairs during the periods of overlapping data, and only retained if at least one month of overlapping data is available. The correlation for each station combination for each variable is then regressed as function of the distance between all station-pairs in Fig. 8. The distances and correlations are also given in Table D1 and Table D2. The largest correlation is found for air temperature (Fig. 8a, green dots), with a fitted e-folding distance of 1430 km, which is defined as the distance where the fitted correlation equals 0.37. This distance is consistent with Bumbaco et al. (2014) and Hakim et al. (2020) that make use of different data. On the other hand, the correlation between stations for horizontal wind speed and for ~~both~~ the two downward radiation components is lower (Fig. 8b), with an e-folding distance of about 500 km for all three variables. It must be noted that such correlations also depend on the region and on the season (Bumbaco et al., 2014). The lower correlation for wind speed and downward radiation confirms the need for a denser array of stations for energy balance applications.

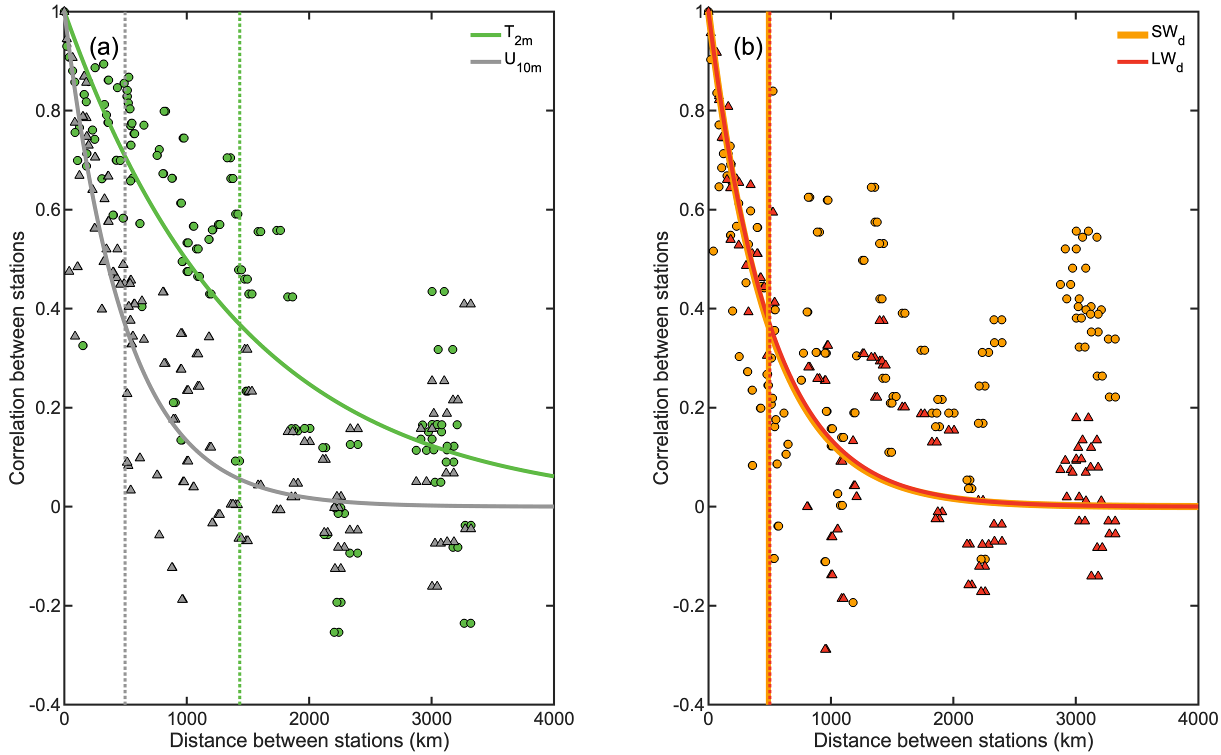

Figure 8. Temporal correlations of daily average (a) air temperature (T, ~~red~~green), horizontal wind speed (U, grey) and (b) downward shortwave radiation (SW_d, ~~yellow~~orange) and downward longwave radiation (LW_d, red) in January between all station-pairs versus the horizontal distance between stations. The lines denote the fit to exponential-decay functions, with the e-folding distance denoted by the vertical dashed lines.

5 Data uncertainties and recommendations

While the corrections presented in Sect. 2.3 are based on short experiments with benchmark datasets, the weather stations have been in operation in remote areas on the Antarctic ice sheet, which prevents a direct comparison of their long-term measurements with independent benchmark datasets. As such, the uncertainty of the final, corrected parameters is estimated as follows. From 2001-01-01 through 2001-10-28, a type I and a type II station were simultaneously operating at AWS10, and from 2015-01-23 through 2015-12-31, a type II and a type III station were simultaneously operational at AWS14. The mean absolute difference (MD) and centred root-mean-square-deviation (RMSD) of the overlapping, 2-hourly (AWS10) and hourly (AWS14) parameters are then computed and reported in Table 5. In addition, we compare the measured horizontal wind speed by the type II station at AWS14 with overlapping sonic anemometer data taken from 2011-01-06 through 2011-01-30, during the experiment described by Kuipers Munneke et al. (2012), and at AWS05 with overlapping sonic anemometer and fine-wire thermocouple data from 2007-01-15 through 2008-07-05. These additional data are not part of this dataset. Finally, we compare both downwards radiation components measured by the type III station at AWS11 with independent reference data from the BSRN site at Neumayer from 2010-02-14 through 2019-01-30 (Schmithüsen, 2021), although these stations are located 80km apart.

On average, the air temperature between stations differs by 0.76 ± 0.91 °C (MD ± RMSD) for stations I & II, and 0.25 ± 0.45 ° for stations II & III, which exceeds the reported accuracy by the manufacturer (0.1 °C for types I & III, 0.3 °C for type II, Table 2). We attribute this larger uncertainty to the different sensor heights, to the different sampling strategy, and to the uncertainty of the excess temperature correction due to the variable effectiveness of the radiation ~~huts~~shields. The comparison with a fine-wire thermocouple at AWS05 also reveals recorded air temperature differences of 0.2 ± 0.64 ◦C, which confirms that the sensors performance is slightly different than reported by the manufacturer.

The difference in measured, corrected relative humidity between stations type II and III (8 % ± 14 %) also exceeds the reported accuracy, which translates in specific humidity differences of 0.15 $\mathrm{gkg^{-1}}$ ± 0.32 $\mathrm{gkg^{-1}}$, which remains limited due to the low temperatures in this dataset . The differences are mainly caused by the relative large uncertainty of the hygrometer readings at low temperatures (minimum of -49.7 °C at AWS14) and different sensor types, but also by different sensor heights and different radiation ~~hut~~ shield types.

The horizontal wind speed does not substantially differ ~~than~~ from the reported manufacturer accuracy, except when comparing type I & II , which we attribute to the different sampling strategy and to the different response and overspeeding of cup anemometers. Further, the cup anemometer at AWS10 was never replaced ~~since~~ after it's installation in 1995. The comparison between type II and sonic anemometer data at AWS05 reveals differences of 0.1 ± 0.85 $\mathrm{ms^{-1}}$, which may be interpreted as the uncertainty in measured wind speed by stations II / III in the polar conditions from this dataset. We attribute the differences with sonic anemometer readings to different heights, flow distortion, poor response of propeller anemometers at low wind speeds (lower than 1.5 $\mathrm{ms^{-1}}$), and noise in the sonic anemometer readings due to e.g. precipitation, blowing snow in the sensor volume or riming of the transducer heads.

The mean absolute difference of all four radiative components ranges between 1 $\mathrm{Wm^{-2}}$ to 8 $\mathrm{Wm^{-2}}$ between stations. The performance of the Anderaa 2770 sensor used to measure downwards shortwave radiation on the type I stations is lower than reported by the manufacturer, and also lower than the CRN1/4 used on types II and III, with a RMSD value of 34 Wm^{-2} versus 19 Wm^{-2}. On the other hand, we find that the corrected, hourly CNR1/4 readings differ by less than ~~%~~ 5 % of the daily averages, which is better than reported by the manufacturer and consistent with the result from Van den Broeke et al. (2004). It must be noted that the location of AWS10 is more susceptible to frosting, which possibly causes larger downwards shortwave radiation differences compared to other locations, since different radiometers may behave differently under frosting conditions. Despite the 80 km horizontal separation and about 650 m elevation difference, downwards shortwave and longwave radiation measured at AWS11 only differ by on average 11 ± 68 Wm^{-2} and 4 ± 31 Wm^{-2} over a 10-year period, respectively, from the benchmark measurements from the Neumayer BSRN site (Schmithüsen, 2021) . This further supports the high accuracy of the corrected CRN1/4 readings. Small average differences in measured shortwave components may still translate into relatively large error in broadband shortwave albedo, with RMSD values of 0.026 a AWS14 during 2015.

Finally, the intercomparison of the hourly surface height recorded by two different sonic height ranger reveals RMSD values of 0.08 m ~~for~~ between the type I/II stations and 0.04 m between type II/III stations. These values are higher than reported by the manufacturer, which we attribute to the horizontal variability of the snow surface and to noise generated by secondary reflections.

The measurements in this dataset were taken in (or in the vicinity of) Dronning Maud Land and the Larsen C ice shelf, hence different datasets should be included for Antarctic wide studies. This may include other AWS (e.g. Ding et al., 2022; Wang et al., 2023), or SMB (Favier et al., 2013; Wang et al., 2021) compilations, surface meteorological observations from year-round crewed stations, or surface radiation observations from the BSRN network at Neumayer (Schmithüsen, 2021), Concordia (Lupi et al., 2021), South Pole (Riihimaki et al., 2023) and Syowa (Ogawa et al., 2024).

We recommend future Antarctic AWS design to include measurements of the four radiation components and surface height change, which allow for the SEB quantification including melt and therefore for a more complete evaluation of climate models.

Table 5. Estimated mean absolute difference (MD) and centred root-mean-square deviation (RMSD) of hourly measured parameters between two overlapping and independent datasets at five locations.

Comparison between	type I and type II data at AWS10 2001-01-01 / 2001-10-28		type II and type III data at AWS14 2015-01-23 / 2015-12-31		type II and sonic anemometer data at AWS14 2011-01-06 / 2011-01-30		type II and Neumayer BSRN data at AWS11 2010-02-14 / 2019-01-30		type II and sonic anemometer with fine-wire thermocouple data at AWS05 2007-01-15 / 2008-07-05	
variable	MD	RMSD	MD	RMSD	MD	RMSD	MD	RMSD	MD	RMSD
t	0.76°C	0.91°C	0.25 °C	0.45 °C					0.20 °C	0.64 °C
rh			8 %	14 %						
q			0.15 gkg^{-1}	0.32 gkg^{-1}						
wspd	0.2 ms^{-1}	2.2 ms^{-1}	1.1 ms^{-1}	0.8 ms^{-1}	0.7 ms^{-1}	0.5 ms^{-1}			0.1 ms^{-1}	0.85 ms^{-1}
p	132 Pa	58 Pa	26 Pa	45 Pa						
SWd	2 Wm^{-2}	34 Wm^{-2}	8 Wm^{-2}	19 Wm^{-2}			11 Wm^{-2}	68 Wm^{-2}		
SWu			5 Wm^{-2}	14 Wm^{-2}						
LWd			5 Wm^{-2}	6 Wm^{-2}			4 Wm^{-2}	31 Wm^{-2}		
LWu			1 Wm^{-2}	2 Wm^{-2}						
z_surf[1]	0.11 m	0.08 m	0.55 m	0.04 m	0.70 m *				0.22 m *	
alb			0.002	0.026						

* Same sonic height ranger data was used for the surface height change estimation of the sonic anemometer.

6 Summary

A dataset is presented that contains quality-controlled, continuous, (two-)hourly measurements of meteorological quantities, net surface radiation components and surface height change at 19 locations on the Antarctic ice sheet from 1995 through 2022. This dataset differs from other similar datasets containing these stations, such as Jakobs et al. (2020) and Wang et al. (2021), in how quality control and data corrections were implemented, but also in the number of available recorded parameters. The temperature, humidity and radiation data are corrected for commonly documented measurements errors, noise was both manually and automatically removed, and missing data are left empty. In addition, the temperature, humidity and wind at standard heights, as well as the cumulative change in surface height are provided when available. A simple quality flag is provided for further use in e.g. surface energy balance simulations. Despite the remoteness and harsh climatic conditions of these locations, the average success rate of the hourly data is 90 % for the temperature, 84 % for the wind speed, 73 % for the four components of net surface radiation, 67 % for the measured height change and 50 % for all of the hourly data being simultaneously available.

The measurements from these stations have not been assimilated, thereby allowing for an independent benchmarking of reanalysis products. This dataset may also serve as basis for future work that requires in situ observations to study surface-climate interactions on the Antarctic ice sheet.

7 Data availability

The hourly dataset for all 19 AWS stations is available at https://doi.pangaea.de/10.1594/PANGAEA.974080 (Van Tiggelen et al., 2024).

8 Code and data availability

The code used to pre-process and correct measurement of temperature, longwave radiation and relative humidity for the specific instrument combinations used in this dataset is available at https://doi.org/10.5281/zenodo.15101447 (Van Tiggelen et al., 2025a). The code used to apply the other corrections, flag suspicious data and compute new variables is available at https://doi.org/10.5281/zenodo.15058515 (Van Tiggelen et al., 2025b). The surface energy balance model used to compute the quantities at standard heights is available at https://doi.org/10.5281/zenodo.15082295 (Van Tiggelen et al., 2025c).

Table A1. Manual thresholds applied to the dataset after the corrections. [1]This data was also processed with a manual threshold filter with time varying bounds.

variable	min	max	unit
t	-90	30	°C
rh	0	150	%
wspd	0	100	ms^{-1}
wdir	0	360	°
p	500	1100	hPa
SWd	-20	1500	Wm^{-2}
SWu	-20	1000	Wm^{-2}
LWd	50	500	Wm^{-2}
LWu	50	500	Wm^{-2}
z_surf[1]	0.1	30	m
alb	0.1	0.95	-

Appendix A: Manual thresholds

Table B1. Number of hours of valid, non-flagged data per variable and per station. All data denotes the number of hours with all variables being simultaneously non-flagged.

Station	t	wspd	RH	p	SWd	SWu	LWd	LWu	z_boom	all data	total hours
AWS01	856	1089	0	1405	1149	0	0	0	1409	0	1409
AWS02	1258	1183	0	1339	1157	0	0	0	1352	0	1352
AWS03	963	713	0	987	598	0	0	0	991	0	991
AWS04	1832	1718	1827	1832	1828	1828	1830	1830	1745	1626	1832
AWS05	5810	5733	5787	5811	5700	5702	5809	5805	4885	4676	5821
AWS06	4047	4045	4045	4047	3973	3973	4047	4047	4037	3960	4047
AWS07	863	1108	830	1564	1131	1131	772	772	1180	720	1567
AWS08	1819	1754	1814	1819	1060	657	1559	1782	1820	419	1820
AWS09	9009	8568	6822	8872	8576	8577	7984	6242	9010	3683	9048
AWS10	3307	1808	1496	3378	3207	1486	1463	1453	3383	979	3443
AWS11	3899	3375	2246	3927	3767	3769	3582	3564	3866	1518	3955
AWS12	2981	2707	2964	0	2683	2684	1605	429	3001	0	3001
AWS13	2968	64	2943	0	2760	2763	1800	1798	2985	0	2987
AWS14	4778	4589	4721	4758	4543	4540	4776	4776	4381	3966	4779
AWS15	1931	1849	1917	1347	1885	1885	1930	1930	1855	1209	1931
AWS16	3861	4098	3860	3914	4017	4016	3860	3861	4018	3669	4108
AWS17	1798	1769	1725	1798	1798	1798	1796	1796	1793	1687	1798
AWS18	2926	2816	2860	2926	2845	2845	2921	2921	2923	2667	2926
AWS19	415	411	415	415	408	409	415	415	415	404	415
Total	55321	49397	46272	50139	53085	48063	46149	43421	55049	31183	57230

Appendix B: Number of non-flagged data

Appendix C: Station climatology

Table C1: Long term (AVG), summer (DJM) and winter (JJA) averages of the hourly variables in this dataset: air temperature (t), specific humidity (qv), relative humidity (rh), horizontal wind speed (wspd), air pressure (p), downwards shortwave radiation (SWd), upwards shortwave radiation (SWu), downwards longwave radiation (LWd), upward longwave radiation (LWu), broadband shortwave albedo for solar zenith angles lower than 70 degrees (alb) and surface temperature assuming unit emmisivity (Ts). The percentage of valid hourly data is also given for each variable.

Variable		t	qv	rh	wspd	p	SWd	SWu	LWd	LWu	alb	Ts
Unit		$^{\circ}C$	gkg^{-1}	%	ms^{-1}	hPa	Wm^{-2}	Wm^{-2}	Wm^{-2}	Wm^{-2}	-	$^{\circ}C$
AWS01	AVG	-22.3	-	-	6.2	817	149	0	-	-	-	-
	JJA	-27.2	-	-	7.7	815	7	0	-	-	-	-
	DJF	-13.2	-	-	4.8	822	339	0	-	-	-	-
	% data	61	0	0	77	100	85	0	0	0	0	0
AWS02	AVG	-27.8	-	-	6.6	713	151	0	-	-	-	-
	JJA	-31.8	-	-	7.8	710	5	0	-	-	-	-
	DJF	-19.9	-	-	5.0	720	379	0	-	-	-	-
	% data	94	0	0	88	99	92	0	0	0	0	0
AWS03	AVG	-46.4	-	-	4.1	617	231	0	-	-	-	-
	JJA	-56.4	-	-	3.8	615	10	0	-	-	-	-
	DJF	-33.4	-	-	4.3	624	416	0	-	-	-	-
	% data	97	0	0	72	100	95	0	0	0	0	0
AWS04	AVG	-18.9	1.04	94.6	5	979	123	107	216	236	0.88	-18
	JJA	-26.7	0.48	96.1	4.8	980	3	3	199	208	-	-24.9
	DJF	-7	2.09	91.9	4.9	980	285	247	246	281	0.87	-8.2
	% data	100	100	100	100	100	100	100	100	100	18	75
AWS05	AVG	-16.1	1.04	83.0	6.8	943	130	108	204	240	0.84	-18.6
	JJA	-22.9	0.52	84.3	7.3	943	3	3	184	213	-	-25.7
	DJF	-6.9	1.90	80.9	5.4	946	308	254	229	278	0.83	-8.6
	% data	100	99	99	99	100	100	100	100	100	18	80
AWS06	AVG	-20.4	0.75	78.6	6.8	855	137	114	179	224	0.84	-23.9
	JJA	-26.6	0.39	80.1	7.6	853	2	2	165	200	-	-29.6
	DJF	-11.5	1.35	77.0	5.5	860	322	266	201	258	0.83	-13.6
	% data	100	100	100	100	100	100	100	100	100	17	97
AWS07	AVG	-20.3	0.51	61.9	5.7	847	111	69	182	228	0.62	-21.9
	JJA	-26.4	0.29	68.9	6.2	846	4	3	168	205	-	-28.4
	DJF	-9.9	0.90	47.7	4.8	852	274	168	203	270	0.62	-11.0
	% data	55	54	54	71	100	73	73	49	49	12	6
AWS08	AVG	-37.2	0.26	94.8	5.1	719	128	113	149	175	0.82	-37.9
	JJA	-45.1	0.1	97.5	5.5	717	1	1	150	153	-	-41.1
	DJF	-24.4	0.60	89.7	4.4	723	334	294	159	215	0.81	-28.0
	% data	100	100	100	100	100	59	37	86	98	4	16
AWS09	AVG	-41.8	0.19	91.6	4.2	677	147	120	135	161	0.82	-39.5
	JJA	-51.9	0.06	92.1	4.4	673	2	2	135	137	-	-48.3
	DJF	-27.5	0.46	88.6	4.2	682	354	288	142	199	0.82	-30.4
	% data	100	72	74	99	98	100	100	95	73	17	31
AWS10	AVG	-24.3	0.65	96.9	3.4	880	110	98	200	216	0.89	-21.5
	JJA	-31.2	0.28	96.0	2.2	878	3	1	187	190	-	-33.5
	DJF	-14.2	1.36	94.6	4.0	884	279	257	215	253	0.89	-14.8
	% data	96	40	40	61	98	95	41	39	39	6	21
AWS11	AVG	-17.4	0.94	89.7	8.0	902	133	115	212	237	0.87	-20.0

Variable		t	qv	rh	wspd	p	SWd	SWu	LWd	LWu	alb	Ts
Unit		$^{\circ}C$	gkg^{-1}	%	ms^{-1}	hPa	Wm^{-2}	Wm^{-2}	Wm^{-2}	Wm^{-2}	-	$^{\circ}C$
	JJA	-23.4	0.52	91.3	7.7	901	6	5	195	212	-	-26.7
	DJF	-9.2	1.75	87.0	7.1	904	306	264	235	270	0.87	-11.5
	% data	99	56	57	85	99	100	100	91	90	19	33
AWS12	AVG	-52.2	0.11	91.8	4.3	-	168	131	107	131	0.78	-
	JJA	-63.7	0.02	90.2	4.4	-	1	1	109	112	-	-
	DJF	-35.1	0.32	92.4	4	-	401	311	111	169	0.78	-
	% data	99	99	99	92	0	99	99	82	23	16	0
AWS13	AVG	-53.4	0.09	89.0	4.4	-	157	121	100	130	0.76	-
	JJA	-64.3	0.01	88.0	-	-	0	0	106	108	-	-
	DJF	-36.3	0.27	87.9	4.2	-	393	298	100	170	0.76	-
	% data	99	99	99	2	0	99	99	98	98	15	0
AWS14	AVG	-15	1.34	93.1	3.4	985	131	110	233	250	0.85	-14.3
	JJA	-24	0.58	95.5	3	988	10	9	208	216	-	-23.4
	DJF	-4.2	2.51	89.8	3.5	983	276	232	268	294	0.84	-4.8
	% data	100	98	99	100	100	100	100	100	100	20	77
AWS15	AVG	-16	1.28	94.9	3	986	128	114	230	246	0.89	-15.9
	JJA	-24.6	0.54	96.1	2.6	989	9	8	206	214	-	-24.8
	DJF	-4.9	2.47	93.2	3.1	985	273	239	265	289	0.88	-6.0
	% data	100	99	99	100	70	100	100	100	100	20	56
AWS16	AVG	-18.1	0.69	61	4.9	827	189	114	171	218	0.82	-24.7
	JJA	-23.6	0.38	62.2	5.6	824	5	4	154	195	-	-31.3
	DJF	-10.3	1.28	65.5	4.4	832	323	263	200	256	0.82	-14.2
	% data	94	94	94	100	95	100	100	94	94	17	89
AWS17	AVG	-14.9	1.25	91.8	4.1	987	133	109	233	251	0.83	-16.0
	JJA	-23.6	0.56	94.6	4	988	14	11	208	217	0.81	-24.5
	DJF	-4.4	2.44	89.8	3.7	984	278	230	268	295	0.83	-4.8
	% data	100	96	96	100	100	100	100	100	100	22	92
AWS18	AVG	-12.7	1.40	84.9	3	981	128	110	237	256	0.86	-13.2
	JJA	-20.9	0.74	89.1	2.7	984	11	10	213	223	-	-21.8
	DJF	-3.7	2.35	81.0	2.7	980	272	229	268	296	0.85	-4.6
	% data	100	98	98	100	100	100	100	100	100	20	85
AWS19	AVG	-13	1.19	80.8	8	978	160	129	211	257	0.81	-14.1
	JJA	-21.4	0.64	95.0	10	974	5	4	188	223	-	-22.9
	DJF	-4.4	1.83	67.4	4.4	980	321	251	238	292	0.79	-5.3
	% data	100	100	100	100	100	100	100	100	100	22	97

Appendix D: Station distances and correlation

Table D1. Horizontal distance between each station in km.

AWS	02	03	04	05	06	07	08	09	10	11	12	13	14	15	16	17	18	19
01	40	513	634	561	552	544	573	361	1532	358	1172	1640	2423	2406	698	2509	2525	824
02		489	617	541	523	514	536	321	1495	359	1144	1607	2403	2385	698	2490	2505	828
03			962	878	774	758	650	432	1498	816	661	1153	2640	2612	429	2737	2738	576
04				85	229	247	427	541	1094	347	1497	1836	1802	1785	1290	1889	1905	1428
05					162	178	359	456	1103	305	1416	1765	1873	1854	1208	1961	1976	1346
06						18	198	343	1011	398	1270	1604	1914	1890	1135	2008	2016	1279
07							180	327	1011	403	1251	1586	1927	1903	1121	2022	2029	1265
08								251	956	537	1083	1405	2006	1978	1044	2105	2106	1192
09									1197	478	977	1377	2236	2210	805	2331	2336	952
10										1381	1578	1582	1450	1398	1902	1566	1532	2045
11											1447	1865	2123	2110	1056	2204	2226	1181
12												526	2913	2874	814	3018	3003	889
13													2973	2927	1330	3083	3054	1398
14														67	3075	122	108	3215
15															3045	183	141	3186
16																3120	3126	151
17																	86	3320
18																		3323
19																		

Table D2. Temporal correlation of hourly January air temperature between each station with at least one month of overlapping data.

AWS	02	03	04	05	06	07	08	09	10	11	12	13	14	15	16	17	18	19
01	0.91	0.83	0.40	0.66	0.77	0.73	0.75	0.86	0.43	-	-	-	-	-	-	-	-	-
02		0.86	0.57	0.77	0.81	0.84	0.8	0.89	0.46	-	-	-	-	-	-	-	-	-
03			0.5	0.66	0.72	0.71	0.77	0.85	0.23	-	-	-	-	-	-	-	-	-
04				0.86	0.76	0.74	0.70	0.66	0.52	-	-	-	-	-	-	-	-	-
05					0.83	0.82	0.78	0.70	0.47	0.66	0.59	0.56	0.15	0.16	0.56	0.16	-	-
06						0.93	0.86	0.79	0.53	0.59	0.57	0.56	-	-	-	-	-	-
07							0.69	0.81	0.48	-	-	-	-	-	-	-	-	-
08								0.89	0.61	-	-	-	-	-	-	-	-	-
09									0.43	0.58	0.74	0.66	-0.01	0.00	0.67	-0.09	0.13	0.13
10										-	-	-	-	-	-	-	-	-
11											0.48	0.42	-0.06	0.12	0.57	-0.25	-0.19	0.54
12												0.87	0.14	0.11	0.80	0.11	0.43	0.21
13													0.15	0.16	0.7	0.17	0.32	0.09
14														0.88	0.05	0.77	0.70	-0.08
15															0.17	0.71	-	-
16																0.09	0.12	0.33
17																	0.76	-0.24
18																		-0.04
19																		

Author contributions. Data curation: PS, CHR and MVT. Data corrections: PS and MVT. Formal analysis: MVT with the help of all the authors. Writing/Visualisation: MVT with the help of all the authors. Funding: CHR and MRVB with the help of all the authors. Conceptualization/investigation/methodology: all the authors. Project administration: CHR and MRVB.

Competing interests. The authors declare no conflict of interest.

Acknowledgements. The authors thank all the persons involved in the transport, installation, servicing and dismantling of the weather stations. The technical staff of the IMAU is acknowledged for the design of the weather stations. The Alfred Wegener Institute (AWI) is acknowledged for the support regarding the weather stations at Kohnen Base (AWS09), on Berkner Island (AWS10) and on the Halvfarryggen ice rise (AWS11). The installations of weather stations on Plateau station B (AWS12), and the Pole of inaccessibility (AWS13) were carried out under the umbrella of the project Trans-Antarctic Scientific Traverse Expeditions – Ice Divide of East Antarctica (TASTE-IDEA), funded by the Norwegian Polar Institute, the U.S. National Science Foundation (NSF), and the Research Council of Norway within the framework of TASTE-IDEA project 152 of IPY 2007–2008. The installations of AWS01-03 were carried out at a traverse during the Norwegian Antarctic Research Expedition (NARE) 1996/97 organized by the Norwegian Polar Institute. The traverse was a contribution to the ”European Project for Ice Coring in Antarctica” (EPICA), a joint ESF (European Science Foundation)/EC scientific programme, funded by the European Commission under the Environment and Climate Programme (1994-1998) contract ENV4-CT95-0074 and by national contributions from Belgium, Denmark, France, Germany, Italy, The Netherlands, Norway, Sweden, Switzerland and the United Kingdom. The Finnish Antarctic Research Program, (FINNARP) at the Finnish Meteorological Institute (FMI) is acknowledged for the support with the operation of the weather station at Wasa/Aboa Camp Maudheimvida (AWS5). The Royal Meteorological Institute of Belgium (KMI) and the KU Leuven are acknowledged for the support regarding the weather station at the Princess Elisabeth station (AWS16) and On the King Baudouin ice shelf (AWS19). The British Antarctic survey is acknowledged for the support with the operations of the weather stations on the Larsen C ice shelf: North (AWS14), South (AWS15) and Cabinet inlet (AWS18), and on the remnants of the Larsen B ice shelf on Scar inlet (AWS17). The Swedish Antarctic Research Programme (SWEDARP) is acknowledged for the support with the operations of the weather station at the Rampen site 1090 (AWS04), Wasa/Aboa Camp Maudheimvida (AWS05), Svea (AWS06), Scharffenbergbotnen (AWS07), and Camp Victoria (AWS08) in Dronning Maud Land. The weather station on Roi Baudouin ice shelf (AWS19) was installed in the framework of the BENEMELT project, funded by the InBev-Baillet Latour Antarctica Fellowship, a joint initiative of the InBev-Baillet Latour Fund and the International Polar Foundation (IPF). This work is funded by the Dutch Research Council (NWO) projects "Dutch Polar Climate and Cryosphere Change Consortium" (DP4C, number ALWPP.2019.003) and "State and fate of Antarctica's gatekeepers: a HIgh Resolution approach for Ice ShElf instability" (HiRISE, number OCENW.GROOT.2019.091). The authors thank PANGAEA for hosting the dataset.

References

Allison, I.: Surface climate of the interior of the Lambert Glacier basin, Antarctica, from automatic weather station data, Annals of Glaciology, 27, 515–520, https://doi.org/10.3189/1998aog27-1-515-520, 1998.

Amory, C.: Drifting-snow statistics from multiple-year autonomous measurements in Adélie Land, East Antarctica, Cryosphere, 14, 1713–1725, https://doi.org/10.5194/tc-14-1713-2020, 2020.

Anderson: A method for rescaling humidity sensors at temperatures well below freezing, J. Atmos. Ocean. Technol., 11, 1388, https://doi.org/10.1175/1520-0426(1994)011<1388:AMFRHS>2.0.CO;2, 1994.

Andreas, E.: A theory for the scalar roughness and the scalar transfer coefficients over snow and sea ice, Boundary-Layer Meteorol., 38, 159–184, 1986.

Behrens, K.: Radiation Sensors, pp. 297–357, Springer International Publishing, https://doi.org/10.1007/978-3-030-52171-4_11, 2021.

Bintanja, R. and Reijmer, C. H.: Meteorological conditions over Antarctic blue-ice areas and their influence on the local surface mass balance, Journal of Glaciology, 47, 37–50, https://doi.org/10.3189/172756501781832557, 2001.

Bumbaco, K. A., Hakim, G. J., Mauger, G. S., Hryniw, N., and Steig, E. J.: Evaluating the Antarctic observational network with the Antarctic Mesoscale Prediction System (AMPS), Monthly Weather Review, 142, 3847–3859, https://doi.org/10.1175/MWR-D-13-00401.1, 2014.

Buzzard, S., Feltham, D., and Flocco, D.: Modelling the fate of surface melt on the Larsen C Ice Shelf, Cryosphere, 12, 3565–3575, https://doi.org/10.5194/tc-12-3565-2018, 2018.

Ding, M., Zou, X., Sun, Q., Yang, D., Zhang, W., Bian, L., Lu, C., Allison, I., Heil, P., and Xiao, C.: The PANDA automatic weather station network between the coast and Dome A, East Antarctica, Earth System Science Data, 14, 5019–5035, https://doi.org/10.5194/essd-14-5019-2022, 2022.

Drews, R., Martín, C., Steinhage, D., and Eisen, O.: Characterizing the glaciological conditions at Halvfarryggen ice dome, Dronning Maud Land, Antarctica, J. Glaciol., 59, 9–20, https://doi.org/10.3189/2013JoG12J134, 2013.

Dunmire, D., Lenaerts, J. T., Banwell, A. F., Wever, N., Shragge, J., Lhermitte, S., Drews, R., Pattyn, F., Hansen, J. S., Willis, I. C., Miller, J., and Keenan, E.: Observations of Buried Lake Drainage on the Antarctic Ice Sheet, Geophys. Res. Lett., 47, https://doi.org/10.1029/2020GL087970, 2020.

EPICA: Eight glacial cycles from an Antarctic ice core EPICA community members*, Nature, 429, 623–628, www.nature.com/nature, 2004.

EPICA, C.: One-to-one coupling of glacial climate variability in Greenland and Antarctica, Nature, 444, 195–198, https://doi.org/10.1038/nature05301, 2006.

Favier, V., Agosta, C., Parouty, S., Durand, G., Delaygue, G., Gallée, H., Drouet, A. S., Trouvilliez, A., and Krinner, G.: An updated and quality controlled surface mass balance dataset for Antarctica, Cryosphere, 7, 583–597, https://doi.org/10.5194/tc-7-583-2013, 2013.

Goldman, H. V.: From the editor: Halfway through the IPY - Halfway for an Antarctic traverse, Polar Res., 27, 1–6, https://doi.org/10.1111/j.1751-8369.2008.00048.x, 2008.

Gorodetskaya, I. V., Van Lipzig, N. P., Van Den Broeke, M. R., Mangold, A., Boot, W., and Reijmer, C. H.: Meteorological regimes and accumulation patterns at Utsteinen, Dronning Maud Land, East Antarctica: Analysis of two contrasting years, J. Geophys. Res. Atmos., 118, 1700–1715, https://doi.org/10.1002/jgrd.50177, 2013.

Grigioni, P., Ciardini, V., DE SILVESTRI, L., IACCARINO, A., SCARCHILLI, C., CAMPOREALE, G., DOLCI, S., PELLEGRINI, A., PROPOSITO, M., and SCHIOPPO, R.: La rete di stazioni meteorologiche dell'Osservatorio Meteo-Climatologico in Antartide, ENEA, 2016.

Hakim, G. J., Bumbaco, K. A., Tardif, R., and Powers, J. G.: Optimal network design applied to monitoring and forecasting surface temperature in Antarctica, Monthly Weather Review, 148, 857–873, https://doi.org/10.1175/MWR-D-19-0103.1, 2020.

Holmlund, P., Gjerde, K., Gundestrup, N., Hansson, M., Isaksson, E., Karlöf, L., Nman, M., Pettersson, R., Pinglot, F., Reijmer, C. H., Stenberg, M., Thomassen, M., van de Wal, R., van der Veen, C., Wilhelms, F., and Winther, J.-G.: Spatial gradients in snow layering and 10 m temperatures at two EPICA-Dronning Maud Land (Antarctica) pre-site-survey drill sites, Ann. Glaciol., 30, 13–19, https://doi.org/10.3189/172756400781820796, 2000.

Holtslag, A. A. M. and De Bruin, H. A. R.: Applied Modeling of the Nighttime Surface Energy Balance over Land, https://doi.org/10.1175/1520-0450(1988)027<0689:amotns>2.0.co;2, 1988.

Howat, I., Porter, C., Noh, M.-J., Husby, E., Khuvis, S., Danish, E., Tomko, K., Gardiner, J., Negrete, A., Yadav, B., Klassen, J., Kelleher, C., Cloutier, M., Bakker, J., Enos, J., Arnold, G., Bauer, G., and Morin, P.: The Reference Elevation Model of Antarctica - Mosaics, Version 2, https://doi.org/10.7910/DVN/EBW8UC, 2022.

Hu, Z., Kuipers Munneke, P., Lhermitte, S., Izeboud, M., and Van Den Broeke, M.: Improving surface melt estimation over the Antarctic Ice Sheet using deep learning: A proof of concept over the Larsen Ice Shelf, Cryosphere, 15, 5639–5658, https://doi.org/10.5194/tc-15-5639-2021, 2021.

Huwald, H., Higgins, C. W., Boldi, M. O., Bou-Zeid, E., Lehning, M., and Parlange, M. B.: Albedo effect on radiative errors in air temperature measurements, Water Resources Research, 45, 1–13, https://doi.org/10.1029/2008WR007600, 2009.

Jacobs, A. F. and McNaughton, K. G.: The excess temperature of a rigid fast-response thermometer and its effects on measured heat flux, J. Atmos. Ocean. Technol., 11, 680–686, https://doi.org/10.1175/1520-0426(1994)011<0680:TETOAR>2.0.CO;2, 1994.

Jakobs, C. L., Reijmer, C. H., Smeets, C. J., Trusel, L. D., Van De Berg, W. J., Van Den Broeke, M. R., and Van Wessem, J. M.: A benchmark dataset of in situ Antarctic surface melt rates and energy balance, J. Glaciol., 66, 291–302, https://doi.org/10.1017/jog.2020.6, 2020.

Kittel, C., Amory, C., Agosta, C., Jourdain, N. C., Hofer, S., Delhasse, A., Doutreloup, S., Huot, P. V., Lang, C., Fichefet, T., and Fettweis, X.: Diverging future surface mass balance between the Antarctic ice shelves and grounded ice sheet, Cryosphere, 15, 1215–1236, https://doi.org/10.5194/tc-15-1215-2021, 2021.

Knap, W.: Basic and other measurements of radiation at station Cabauw (2005-02 et seq), https://doi.org/10.1594/PANGAEA.940531, 2022.

Kuipers Munneke, P., Van Den Broeke, M. R., King, J. C., Gray, T., and Reijmer, C. H.: Near-surface climate and surface energy budget of Larsen C ice shelf, Antarctic Peninsula, Cryosphere, 6, 353–363, https://doi.org/10.5194/tc-6-353-2012, 2012.

Kuipers Munneke, P., Luckman, A. J., Bevan, S. L., Smeets, C. J. P. P., Gilbert, E., van den Broeke, M. R., Wang, W., Zender, C., Hubbard, B., Ashmore, D., Orr, A., King, J. C., and Kulessa, B.: Intense Winter Surface Melt on an Antarctic Ice Shelf, Geophys. Res. Lett., 45, 7615–7623, https://doi.org/10.1029/2018GL077899, 2018.

Kurita, N., Kameda, T., Motoyama, H., Hirasawa, N., Mikolajczyk, D., Welhouse, L. J., Keller, L. M., Weidner, G. A., and Lazzara, M. A.: Near-Surface Air Temperature Records over the Past 30 Years in the Interior of Dronning Maud Land, East Antarctica, Journal of Atmospheric and Oceanic Technology, 41, 179–188, https://doi.org/10.1175/JTECH-D-23-0092.1, 2024.

Laepple, T., Werner, M., and Lohmann, G.: Synchronicity of Antarctic temperatures and local solar insolation on orbital timescales, Nature, 471, 91–94, https://doi.org/10.1038/nature09825, 2011.

Lazzara, M. A., Weidner, G. A., Keller, L. M., Thom, J. E., and Cassano, J. J.: Antarctic automatic weather station program: 30 years of polar observations, Bull. Am. Meteorol. Soc., 93, 1519–1537, https://doi.org/10.1175/BAMS-D-11-00015.1, 2012.

Le Moigne, P., Bazile, E., Cheng, A., Dutra, E., Edwards, J. M., Maurel, W., Sandu, I., Traullé, O., Vignon, E., Zadra, A., and Zheng, W.: GABLS4 intercomparison of snow models at Dome C in Antarctica, Cryosphere, 16, 2183–2202, https://doi.org/10.5194/tc-16-2183-2022, 2022.

Lenaerts, J. T., Lhermitte, S., Drews, R., Ligtenberg, S. R., Berger, S., Helm, V., Smeets, C. J., Broeke, M. R. D., Van De Berg, W. J., Van Meijgaard, E., Eijkelboom, M., Eisen, O., and Pattyn, F.: Meltwater produced by wind-albedo interaction stored in an East Antarctic ice shelf, Nature Climate Change, 7, 58–62, https://doi.org/10.1038/nclimate3180, 2017.

Lupi, A., Lanconelli, C., and Vitale, V.: Basic and other measurements of radiation at Concordia station (2006-01 et seq), https://doi.org/10.1594/PANGAEA.935421, 2021.

Makkonen, L. and Laakso, T.: Humidity measurements in cold and humid environments, Boundary-Layer Meteorology, 116, 131–147, https://doi.org/10.1007/s10546-004-7955-y, 2005.

Morlighem, M., Rignot, E., Binder, T., Blankenship, D., Drews, R., Eagles, G., Eisen, O., Ferraccioli, F., Forsberg, R., Fretwell, P., Goel, V., Greenbaum, J. S., Gudmundsson, H., Guo, J., Helm, V., Hofstede, C., Howat, I., Humbert, A., Jokat, W., Karlsson, N. B., Lee, W. S., Matsuoka, K., Millan, R., Mouginot, J., Paden, J., Pattyn, F., Roberts, J., Rosier, S., Ruppel, A., Seroussi, H., Smith, E. C., Steinhage, D., Sun, B., den Broeke, M. R., Ommen, T. D., van Wessem, M., and Young, D. A.: Deep glacial troughs and stabilizing ridges unveiled beneath the margins of the Antarctic ice sheet, Nature Geoscience, 13, 132–137, https://doi.org/10.1038/s41561-019-0510-8, 2020.

Mottram, R., Hansen, N., Kittel, C., Van Wessem, J. M., Agosta, C., Amory, C., Boberg, F., Van De Berg, W. J., Fettweis, X., Gossart, A., Van Lipzig, N. P., Van Meijgaard, E., Orr, A., Phillips, T., Webster, S., Simonsen, S. B., and Souverijns, N.: What is the surface mass balance of Antarctica? An intercomparison of regional climate model estimates, vol. 15, https://doi.org/10.5194/tc-15-3751-2021, 2021.

Nakamura, R. and Mahrt, L.: Air temperature measurement errors in naturally ventilated radiation shields, Journal of Atmospheric and Oceanic Technology, 22, 1046–1058, https://doi.org/10.1175/JTECH1762.1, 2005.

Ogawa, Y., Tanaka, Y., Ogihara, H., Fukuda, M., Kawashima, K., Doi, M., and Yamanouchi, T.: Basic and other measurements of radiation at station Syowa (1994-01 et seq) , https://doi.org/10.1594/PANGAEA.956748, 2024.

Reijmer, C., Greuell, W., and Oerlemans, J.: The annual cycle of meteorological variables and the surface energy balance on Berkner Island, Antarctica, Ann. Glaciol., 29, 49–54, https://doi.org/10.3189/172756499781821166, 1999.

Reijmer, C. H. and van den Broeke, M. R.: Temporal and spatial variability of the surface mass balance in Dronning Maud Land, Antarctica, as derived from automatic weather stations, J. Glaciol., 49, 512–520, https://doi.org/10.3189/172756503781830494, 2003.

Riihimaki, L., Long, C. E., Dutton, E. G., and Michalsky, J.: Basic and other measurements of radiation at station South Pole (1992-01 et seq), https://doi.org/10.1594/PANGAEA.956847, 2023.

Schmithüsen, H.: Basic and other measurements of radiation at Neumayer Station (1992-04 et seq), https://doi.org/10.1594/PANGAEA.932418, 2021.

Smeets, P. C. J. P., Kuipers Munneke, P., van As, D., van den Broeke, M. R., Boot, W., Oerlemans, H., Snellen, H., Reijmer, C. H., and van de Wal, R. S. W.: The K-transect in west Greenland: Automatic weather station data (1993–2016), Arctic, Antarct. Alp. Res., 50, S100 002, https://doi.org/10.1080/15230430.2017.1420954, 2018.

Souverijns, N., Gossart, A., Demuzere, M., Lenaerts, J. T., Medley, B., Gorodetskaya, I. V., Vanden Broucke, S., and van Lipzig, N. P.: A New Regional Climate Model for POLAR-CORDEX: Evaluation of a 30-Year Hindcast with COSMO-CLM 2 Over Antarctica, Journal of Geophysical Research: Atmospheres, 124, 1405–1427, https://doi.org/10.1029/2018JD028862, 2019.

Thiery, W., Gorodetskaya, I. V., Bintanja, R., Van Lipzig, N. P., Van Den Broeke, M. R., Reijmer, C. H., and Kuipers Munneke, P.: Surface and snowdrift sublimation at Princess Elisabeth station, East Antarctica, Cryosphere, 6, 841–857, https://doi.org/10.5194/tc-6-841-2012, 2012.

Trusel, L. D., Frey, K. E., Das, S. B., Munneke, P. K., and Van Den Broeke, M. R.: Satellite-based estimates of Antarctic surface meltwater fluxes, Geophys. Res. Lett., 40, 6148–6153, https://doi.org/10.1002/2013GL058138, 2013.

Turner, J., Lu, H., White, I., King, J. C., Phillips, T., Hosking, J. S., Bracegirdle, T. J., Marshall, G. J., Mulvaney, R., and Deb, P.: Absence of 21st century warming on Antarctic Peninsula consistent with natural variability, Nature, 535, 411–415, https://doi.org/10.1038/nature18645, 2016.

van Dalum, C. T., van de Berg, W. J., Gadde, S. N., van Tiggelen, M., van der Drift, T., van Meijgaard, E., van Ulft, L. H., and van den Broeke, M. R.: First results of the polar regional climate model RACMO2.4, EGUsphere, 2024, 1–36, https://doi.org/10.5194/egusphere-2024-895, 2024.

Van den Broeke, M., van As, D., Reijmer, C., and van de Wal, R.: Assessing and Improving the Quality of Unattended Radiation Observations in Antarctica, J. Atmos. Ocean. Technol., 21, 1417–1431, https://doi.org/10.1175/1520-0426(2004)021<1417:AAITQO>2.0.CO;2, 2004.

Van den Broeke, M. R., Winther, J. G., Isaksson, E., Pinglot, J. F., Karlöf, L., Eiken, T., and Conrads, L.: Climate variables along a traverse line in Dronning Maud Land, East Antarctica, J. Glaciol., 45, 295–302, https://doi.org/10.3189/s0022143000001799, 1999.

Van Liefferinge, B., Pattyn, F., Cavitte, M. G., Karlsson, N. B., Young, D. A., Sutter, J., and Eisen, O.: Promising oldest ice sites in east antarctica based on thermodynamical modelling, Cryosphere, 12, 2773–2787, https://doi.org/10.5194/tc-12-2773-2018, 2018.

Van Tiggelen, M., Smeets, P. C., Reijmer, C. H., van den Broeke, M. R., van As, D., Box, J. E., and Fausto, R. S.: Observed and Parameterized Roughness Lengths for Momentum and Heat Over Rough Ice Surfaces, J. Geophys. Res. Atmos., 128, https://doi.org/10.1029/2022JD036970, 2023.

Van Tiggelen, M., Smeets, P. C. J. P., Reijmer, C. H., Kuipers Munneke, P., van den Broeke, M. R., Oerter, H., Eisen, O., Steinhage, D., Kipfstuhl, S., van Lipzig, N. P. M., Mangold, A., Lhermitte, S., and Lenaerts, J. T. M.: IMAU Antarctic automatic weather station data, including surface radiation balance (1995-2022), https://doi.org/0.1594/PANGAEA.974080, 2024.

Van Tiggelen, M., Smeets, P. C. J. P., Reijmer, C. H., Kuipers Munneke, P., and van den Broeke, M. R.: MATLAB scripts used to process the IMAU Antarctic automatic weather station data, including surface radiation balance (1995-2022), https://doi.org/10.5281/zenodo.15101447, 2025a.

Van Tiggelen, M., Smeets, P. C. J. P., Reijmer, C. H., Kuipers Munneke, P., and van den Broeke, M. R.: IMAU-ice-and-climate/IMAU-IceEddie, https://doi.org/10.5281/zenodo.15058514, 2025b.

Van Tiggelen, M., Smeets, P. C. J. P., Reijmer, C. H., Kuipers Munneke, P., and van den Broeke, M. R.: IMAU-ice-and-climate/IMAU-pyEBM, https://doi.org/10.5281/zenodo.15082294, 2025c.

Van Wessem, J. M., Van De Berg, W. J., Noël, B. P., Van Meijgaard, E., Amory, C., Birnbaum, G., Jakobs, C. L., Krüger, K., Lenaerts, J. T., Lhermitte, S., Ligtenberg, S. R., Medley, B., Reijmer, C. H., Van Tricht, K., Trusel, L. D., Van Ulft, L. H., Wouters, B., Wuite, J., and Van den Broeke, M. R.: Modelling the climate and surface mass balance of polar ice sheets using RACMO2 - Part 2: Antarctica (1979-2016), Cryosphere, 12, 1479–1498, https://doi.org/10.5194/tc-12-1479-2018, 2018.

Wang, W., Zender, C. S., van As, D., Smeets, P. C. J. P., and van den Broeke, M. R.: A Retrospective, Iterative, Geometry-Based (RIGB) tilt-correction method for radiation observed by automatic weather stations on snow-covered surfaces: application to Greenland, The Cryosphere, 10, 727–741, https://doi.org/10.5194/tc-10-727-2016, 2016.

Wang, Y., Ding, M., Reijmer, C. H., Smeets, P. C., Hou, S., and Xiao, C.: The AntSMB dataset: A comprehensive compilation of surface mass balance field observations over the Antarctic Ice Sheet, Earth System Science Data, 13, 3057–3074, https://doi.org/10.5194/essd-13-3057-2021, 2021.

Wang, Y., Zhang, X., Ning, W., Lazzara, M. A., Ding, M., Reijmer, C. H., Smeets, P. C. J. P., Grigioni, P., Heil, P., Thomas, E. R., Mikolajczyk, D., Welhouse, L. J., Keller, L. M., Zhai, Z., Sun, Y., and Hou, S.: The AntAWS dataset: a compilation of Antarctic automatic weather station observations, Earth Syst. Sci. Data, 15, 411–429, https://doi.org/10.5194/essd-15-411-2023, 2023.

Wever, N., Keenan, E., Amory, C., Lehning, M., Sigmund, A., Huwald, H., and Lenaerts, J. T. M.: Observations and simulations of new snow density in the drifting snow-dominated environment of Antarctica, Journal of Glaciology, pp. 1–18, https://doi.org/10.1017/jog.2022.102, 2022.

Winther, J., van den Broeke, M., Conrads, L., Eiken, T., Hurlen, R., Johnsrud, G., Karlöf, L., Onarheim, S., Richardson, C., and Schorno, R.: EPICA Dronning Maud Land pre site survey 1996/97, Report of the Norwegian Antarctic Research Expedition 1996, 97, 96–114, 1997.

WMO: Guide to Instruments and Methods of Observation Volume I – Measurement of Meteorological Variables, https://library.wmo.int/idurl/4/68695, 2023.